Vat photopolymerization of polylactic acid/hydroxyapatite scaffolds with a unique combination of structural and compositional gradient for multiple-tissue regeneration

Applied Materials Today 46 (2025) 102872

Contents lists available at ScienceDirect

Applied Materials Today

journal homepage: www.elsevier.com/locate/apmt

# Vat photopolymerization of polylactic acid/hydroxyapatite scaffolds with a unique combination of structural and compositional gradient for multiple-tissue regeneration

Zahid Abbas [a], Jeevankumar Pallagani [a], Annalisa La Gatta [b], Chiara Schiraldi [b], Paola Palmero [a], Bartolomeo Coppola [a,*]

[a] Politecnico di Torino, Department of Applied Science and Technology, INSTM R.U. Lince Laboratory, Corso Duca Degli Abruzzi, 24, Italy
[b] Department of Experimental Medicine, Section of Biotechnology, University of Campania "Luigi Vanvitelli", 80138, Naples, Italy

ARTICLE INFO

*Keywords:*
Vat photopolymerization
Compositionally and structurally graded scaffold
Polylactic acid
Hydroxyapatite
Mechanical properties

ABSTRACT

Digital Light Processing (DLP) is a promising approach to fabricate scaffolds with structural and compositional gradients tailored to site-specific tissue properties. In this study, both uniformly dense and gyroid samples as well as structurally graded gyroid scaffolds were designed based on triply periodic minimal surfaces (TPMS) and fabricated by DLP using polylactic acid/hydroxyapatite (PLA/HA) composite slurries. Ultrafine HA powders were added to a commercial PLA resin at 35 wt% and 55 wt%. To produce graded samples, these two slurries were blended in specific ratios (42 and 48 wt%) using a multi-head peristaltic pump, feeding the printer with progressively higher HA contents.

Rheological and curing depth tests confirmed good printability across all slurry compositions, including the highest HA loading. The feasibility of the approach was first demonstrated using dense cylindrical specimens. Microstructural and elemental analyses confirmed the desired compositional gradient, while physical and mechanical tests showed that graded samples had intermediate density, compressive strength, and modulus compared to uniform reference samples.

This approach was further applied to gyroid-type scaffolds, which also demonstrated smooth compositional transitions and similar intermediate mechanical behavior. Preliminary biological assessments confirmed no cytotoxic effects for both neat PLA and PLA/HA composites.

Finally, leveraging the variable HA content slurry, a compositionally and structurally graded PLA/HA gyroid scaffold was printed for the first time, demonstrating the feasibility of the strategy to obtain scaffolds potentially customizable for any type of complex and multilayered anatomical defects.

## 1. Introduction

The application of additive manufacturing (AM) technologies to the fabrication of biomedical scaffolds is opening the field to unprecedented advantages, such as the customization of the implant to individual patients' anatomical defects [1,2], as well as a unique control over scaffold inner architecture [3]. This last advantage becomes pivotal, especially for scaffolds designed to regenerate complex or multi-layer tissues. To make practical examples, human skin is a complex multi-layered system, consisting of the epidermis, dermis and underlying hypodermis, each layer having distinct mechanical properties [4]. Other examples are the so-called "interface tissues" such as tendon-to-bone, cartilage-to-bone, and ligament-to-bone interfaces, located between different types of tissues and connecting layers having different structures, properties and functionalities [5]. Tendon-to-bone insertion, for instance, consists of a ligament that connects two extremely different tissues across a millimeter-wide region: on one side, the soft tissue of the tendon and on the other side, the hard and stiff tissue of bone. Similarly, the osteochondral junction connects the articular cartilage to the subchondral bone, these two tissues being characterized by different compositions, mechanical properties and permeability features.

For such complex tissues, scaffolds need to be engineered to match the physical and biomechanical features of the different layers, with a gradual transition among the layers, and promoting healing and

* Corresponding author at: Department of Applied Science and Technology, Corso Duca Degli Abruzzi, 24, Italy.
*E-mail address:* bartolomeo.coppola@polito.it (B. Coppola).

https://doi.org/10.1016/j.apmt.2025.102872
Received 7 April 2025; Received in revised form 24 July 2025; Accepted 31 July 2025
Available online 7 August 2025

boosting regeneration of all the tissues and their metabolic functions.

Such a challenge cannot be satisfied by single-phase scaffolds, leading to their rapid evolution into bi/tri-layer graded structures to better guide the regeneration of complex hierarchical tissues. Several traditional techniques such as freeze drying [6], salt leaching [7], solvent casting [8] and gas foaming [9], are widely used to provide discrete graded scaffolds, made by separate layers joined together, with inherent discontinuities across the different layers [10]. Transition layers can act as physical barriers, inhibiting the vascularization of the whole construct, while the abrupt changes between layers frequently led to delamination and tissue separation during loading [11]. Furthermore, traditional fabrication techniques typically require multi-step processing to produce graded scaffolds. An example is given in [12], where tri-layered based on layers of collagen/hyaluronic/hydroxyapatite in varying amounts were first separately produced and then stacked together via freeze-drying. Similarly, Amann et al. [13] fabricated tri-layer scaffolds for osteochondral disease made of chitosan-collagen-octacalcium phosphate (OCP), with collagen concentration increasing from the bone to the cartilage layer, and OCP displaying the opposite trend. Each layer-specific solution or suspension was sequentially poured into a mold and frozen, requiring repetition of the process for each layer.

AM technologies have revolutionized the design and fabrication process of functionally graded scaffolds, providing tunable and even continuous gradation of structure and properties [14]. This represents a significant advantage, as the smooth transition and/or the structural continuity between layers enhance interfacial stability while enabling improved load transfer [7,15]. In the context of osteochondral defect reconstruction, this advantage was demonstrated in numerous studies highlighting the superior performance of continuous gradient scaffolds compared to monolithic and bi-layered counterparts [7,16–18].

Among the different AM approaches, vat photopolymerization techniques, including stereolithography (SL) and digital light processing (DLP), have the advantages of highest accuracy [10]. In fact, it is possible to achieve complete control over the architecture inner geometrical features (cells size, distribution, geometry), as never met by other techniques. In this frame, spatial lattice structures such as triply periodic minimal surfaces (TPMS) are gaining increasing success in tissue engineering, as they can be designed with very high surface area-to-volume ratio and pore interconnectivity, leading to high permeability by fluids and cells [19]. By simply modifying the spatial arrangement and size of the cells, a continuous modulation of structural features can be easily achieved. TPMS structures, in fact, are designed by mathematical trigonometric functions, meaning that in the design of a given property, such as density, can be modified as a continuous function in the space, providing a tunable modification in the lattice structure, thus making the goal to fabricate scaffold with a continuous/adjustable gradation fully achievable.

On the other hand, achieving a compositional gradation is more challenging, despite the availability of advanced stereolithography (SL) and digital light processing (DLP) systems equipped with multi-ink dispensing capabilities [20]. However, they typically only achieve discrete gradients using separate printheads to vary compositions. Further, to the best of the authors' knowledge, no previous studies dealing with combined structural and compositional gradients in SL and DLP processed materials are currently available in literature.

Considering the photopolymerizable polymers suitable for SL and DLP, polylactic acid (PLA) is favored for its excellent biocompatibility and its ability to safely excrete degradation by-products [21,22]. Moreover, PLA demonstrates significantly higher mechanical strength compared to most polymers employed in the biomedical field [23,24], making it suitable especially for orthopedic applications. Major drawbacks of PLA are hydrophobicity and no bioactivity, meaning poor wettability and interaction with cells, and no ability to guide the regeneration of damaged tissue. A successful approach to overcome this issue is the incorporation of hydrophilic ceramic particles, such as calcium phosphate (e.g. hydroxyapatite, HA, and α/β-tricalcium phosphates [25], and calcium-containing silicates particles, such as akermanite and baghdadite [26,27]. Considering calcium phosphates, hydroxyapatite (HA) offers exceptional biocompatibility, bioactivity, and osteoconductive properties [28–30]. Zimina et al. [31] demonstrated a clear increase in water wettability moving from pure PLA to PLA/HA composite, as well as a higher adhesion of multipotent mesenchymal stromal cells over the surface of the composite scaffold. Wang et al. [32] used scaffolds incubated *in-vitro* with rabbit bone marrow mesenchymal stem cells (BMSCs) and demonstrated a better biocompatibility of PLA/50wt%HA compared to neat PLA. Further, by *in-vivo* experiment, the composite showed a higher degree of new bone formation, where new bone generated by PLA group at the third month after surgery was comparable to that of composite material group at the first month. In addition, HA can neutralize the acidity of the lactic acid produced after PLA degradation [33] and decrease the risk of inflammatory response.

In this work, the DLP fabrication of PLA/HA compositionally and structurally graded scaffolds is demonstrated for the first time.

First, compositionally graded samples were fabricated at increasing amounts of HA particles in the polymer matrix. To this aim, slurries at different solid loadings were prepared: according to previous literature studies focused on optimized biological properties of PLA/HA composites [34–36] as well as to match an optimal range of viscosity and printability conditions, a minimum (35 wt%) and a maximum (55 wt%) solid loadings were defined; then, by mixing them, slurries at intermediate HA contents were obtained. A multi-head automatic peristaltic pump was used to mix the slurries at the different HA contents and to feed the DLP vessel, allowing to print samples characterized by variable amounts (from 35 to 55 wt%) of HA particles within the PLA matrix. Physical and mechanical properties of uniform samples (i.e., at single solid loadings of 35 wt% and 55 wt%) were compared to those of compositionally graded samples. Specimens with simple cylindrical dense geometries were first developed, to fulfill the specification for compressive tests; secondly, gyroid structures were fabricated, having single and graded compositions. Finally, a gyroid having a continuous structural gradient was designed and successfully printed by using the variable-amount HA slurry. In this way, the feasibility to obtain, in a single printing job, a joined compositional and structural gradation into the scaffold is fully demonstrated, paving the way to the full customization of scaffolds for any type of complex, continuous and multi-layer tissues. Scaffold hydration in a physiological environment and cytotoxicity were also tested to preliminary assess their suitability for tissue engineering purposes.

## 2. Materials and methods

### 2.1. Materials

Commercial HA powder (Captal R, provided by Plasma Biotal, UK) and commercial photo-polymerizable polylactic acid resin (PLA transparent resin, UniFormation, Shenzhen, China) were used as the starting materials. HA powder meets the high-purity biomedical grade standards and complies with ISO 13779–6 2015 'Implants for surgery' [37]. X-ray diffraction analysis performed on the as-received HA powder (not shown) allowed to associate all the peaks to the hydroxyapatite phase, according to the ICDD PDF n. 72–1243 [38]. Polylactic acid (PLA) is a biodegradable resin derived from plants, exhibiting biocompatible characteristics, as claimed by the supplier [39].

A commercial dispersant (Disperbyk-111, BYK Chemie, Germany) was utilized to enhance the ceramic solid loading and promote powder dispersion within the PLA matrix.

Dulbecco's Phosphate Buffered Saline (PBS) without calcium and magnesium was purchased from Corning, USA. Dulbecco's Modified Eagle's Medium (DMEM) and all the reagents for cell culture were obtained from Gibco (Thermofisher Scientific, Waltham, MA, USA).

A human dermal fibroblasts cell line immortalized with hTERT (HDF cells, BJ-5ta, ATCC CRL 4001) was cultured in DMEM containing 4 g/L of glutamine and supplemented with 0.01 mg/mL hygromycin B supplemented with 10 % FBS (v/v) (ThermoFisher Scientific, Rome, Italy).

### 2.2. HA processing and slurry preparation

HA powder was milled in aqueous medium by using 2 mm zirconia spheres (Tosoh Corporation). Ball milling was carried out for several hours, to achieve a fine and constant particle size. The use of zirconia spheres with high crushing strength, allowed to prevent contamination, as demonstrated through X-ray diffraction (XRD) and Energy Dispersive Spectroscopy (EDX) analyses performed on the milled HA powder and on polymer/HA composites.

Initially, photocurable slurries were prepared by incorporating milled HA powders at two different solid loadings: 35 wt% and 55 wt%. The dispersant amount was optimized for each formulation, resulting in optimal values of 6 wt% and 10 wt% (relative to dry powder) for 35 wt% HA and 55 wt% slurries, respectively

HA powder was gradually added in liquid PLA containing the optimized amount of dispersant, in order to achieve satisfactory rheological properties. Slurries were then blended through planetary milling at a speed of 400 rpm for 3 h using agate spheres (∅ = 10 mm). Prior to the printing process, all slurries underwent deaeration under vacuum for 30 min.

### 2.3. Design, printing and post-treatments

Dense cylinder shape intended for compressive tests was designed using MSLattice (MATLAB) software with dimensions of 12.7 × 6.35 mm ($H \times D$) as per applicable standards (ISO 604:2002) for polymer/ceramic composite, as depicted in Fig. 1a [40]. Then, the uniform and graded gyroids based on triply periodic minimal surfaces (TPMS) were designed, where the former is characterized by the same cell dimension all over the cylindrical body (Fig. 1b), and the latter is characterized by a change in the cell parameters, from one basis to the other (Fig. 1c). Dense cylinder design involved zero-unit cells composed of uniform TPMS-based structures, while gyroid structure were designed through a functional TPMS grading sheet-based approach with uniform cell size. Graded structures were designed with a functional TPMS grading solid network-based design which incorporated variations in initial and final cell size. Design parameters for uniform dense and gyroid as well as structurally graded samples are displayed in Fig. 1. For this work, the porosity of dense and gyroid TPMS structural models was set as 0 % and 80 %, respectively.

Samples were printed using a DLP equipment (ADMAFLEX 130, ADMATEC Europe BV, Netherlands) [41]. This DLP apparatus is equipped with a tape sliding at customizable speeds ranging from 10 to 20 mm/s, on which the photosensitive slurry is spread by a blade. By considering a constant slurry thickness of 125 μm, the shear rate applied in printing processes was determined to fall within the range of 80 to 160 $s^{-1}$. Indeed, the shear rate (τ) can be determined using the subsequent equation:

$$\tau = \frac{V}{h} \tag{1}$$

Where V is the velocity of the relative motion, and h is the slurry thickness (125 μm in this study). Optimization of the key printing variables such as exposure time and LED power was done in order to attain high-quality printing outcomes.

In the initial series of experiments, uniform specimens were fabricated using slurries at 35 wt% HA (at 6 wt% dispersant) and at 55 wt% HA (at 10 wt% dispersant).

Next, compositionally graded specimens were fabricated by mixing 35 and 55 wt% HA slurries, using a controlled multi-head automatic

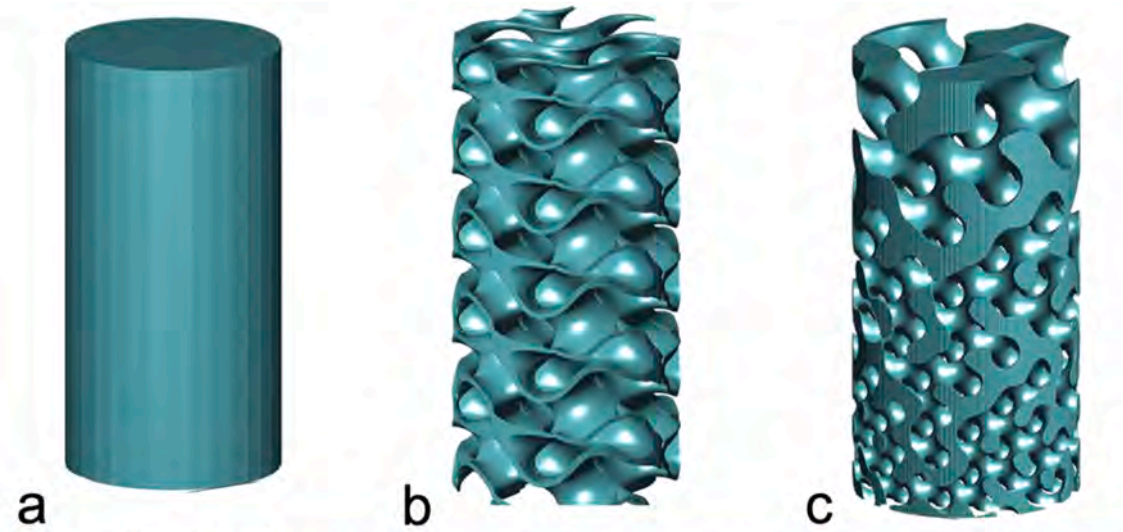


| Figure | Relative density (1-100%) | Radius (mm) | Height (mm) | Initial cell size (mm) | Final cell size (mm) | Mesh density |
|---|---|---|---|---|---|---|
| a | 100 | 3.17 | 12.7 | 0 | 0 | 40 |
| b | 20 | 3.17 | 12.7 | 1.5 | 1.5 | 40 |
| c | 50 | 3.17 | 12.7 | 1.2 | 4 | 40 |

**Fig. 1.** Designed models of samples (a) uniform dense cylinder, (b) uniform gyroid and (c) structurally graded gyroid.

peristaltic pump (Fig. 2) to produce four distinct compositional regions (35, 42, 48, 55 wt% HA powder) inside the samples. Initially, the DLP vessel was filled with the 55 wt% slurry to print the first set of layers. Next, a 65:35 mixture of the 55 wt% and 35 wt% HA slurries was prepared using the multi-head peristaltic pump, resulting in a 48 wt% HA slurry, poured in the vessel and used to print the subsequent set of layers. A total of 105 layers were printed for each HA concentration, with the second slurry being introduced before every set of 10 layers of the previous slurry. This method was employed to generate an intermediate region between two regions, thereby to avoid abrupt changes in composition between the four different parts and obtain an almost continuous compositional gradation. Then, a 35:65 mixture of the same slurries was prepared to yield a 42 wt% HA slurry, which was used for the next set of layers. Finally, the remaining layers were printed using the 35 wt% HA slurry.

Once optimized for the dense samples, the same process was transferred to the gyroid-shape ones, to obtain compositional gradients into complex-shape scaffold-like materials. More precisely, the process was applied to both uniform and compositionally graded gyroids where, in the latter case, a gradient in both composition and structure was successfully obtained.

For the sake of clarity, printed samples were labeled with a code indicating the composition and the structure, as displayed in Table 1.

The fabrication process involved setting the layer thickness to 30 μm, while the curing depth-to-layer thickness ratio (CD/LT) was adjusted between 6.5 and 7.0, by varying printing parameters. Additional printing parameters such as energy dose and exposure time were precisely adjusted to ensure uniform CD across slurries with varying solid loading. The attenuation of energy caused by the PLA/HA resin can be elucidated by the Beer-Lambert law:

$$Ez = E0\ exp\left(\frac{-z}{Dp}\right) \quad (2)$$

Where $E_0$ represents the energy dose at the top of the printing layer, z signifies the depth below the surface (irradiation depth), and Dp denotes the penetration depth within the slurry [42]. As per Eq. (2), the energy dose at a specific depth z (Ez) experiences an exponential decrease as the distance from the surface increases. It was observed that this energy attenuation was more pronounced with higher energy doses. Varied energy doses at distinct depths lead to diverse levels of polymerization, potentially resulting in microstructural defects due to residual stresses [43].

**Table 1**
Schematization of samples code for different sample compositions and structure types.

| Code | Structure type | Sample labels (description) |
|---|---|---|
| *ud* | uniform dense | PLA_*ud* (pure PLA polymer, with no HA addition)<br>PLA/HA_35 wt%_*ud* (composites at constant amounts of HA_35 wt%)<br>PLA/HA_55 wt%_*ud* (composites at constant amounts of HA_55 wt%) |
| *gd* | graded dense (compositional) | PLA/HA_35–55 wt%_*gd* (composites at variable amount of HA, from 35 wt% to 55 wt%) |
| *ug* | uniform gyroid | PLA_*ug* (pure PLA polymer with no HA addition)<br>PLA/HA_35 wt%_*ug* (composites at constant amounts of HA_35 wt%)<br>PLA/HA_55 wt%_*ug* (composites at constant amounts of HA_55 wt%) |
| *gg* | graded gyroid (compositional) | PLA/HA_35–55 wt%_*gg* (composites at variable amount of HA, from 35 wt% to 55 wt%) |
| *sgg* | structure (and compositional) graded gyroid | PLA/HA_35–55 wt%_*sgg* (composites at variable amount of HA, from 35 wt% to 55 wt% as well as graded cellular structure) |

The printed specimens were cleansed with ethanol to remove the surface uncured slurry, and then with deionized water to remove ethanol traces. Following this, the specimens were dried at room temperature overnight, followed by oven-drying at 60 °C for 2 h.

Some samples were also debinded at 650 °C for 1 h (heating rate of 0.1 °C/min up to 380 °C, and then at 1 °C/min up to 650 °C), and submitted to microstructural characterization.

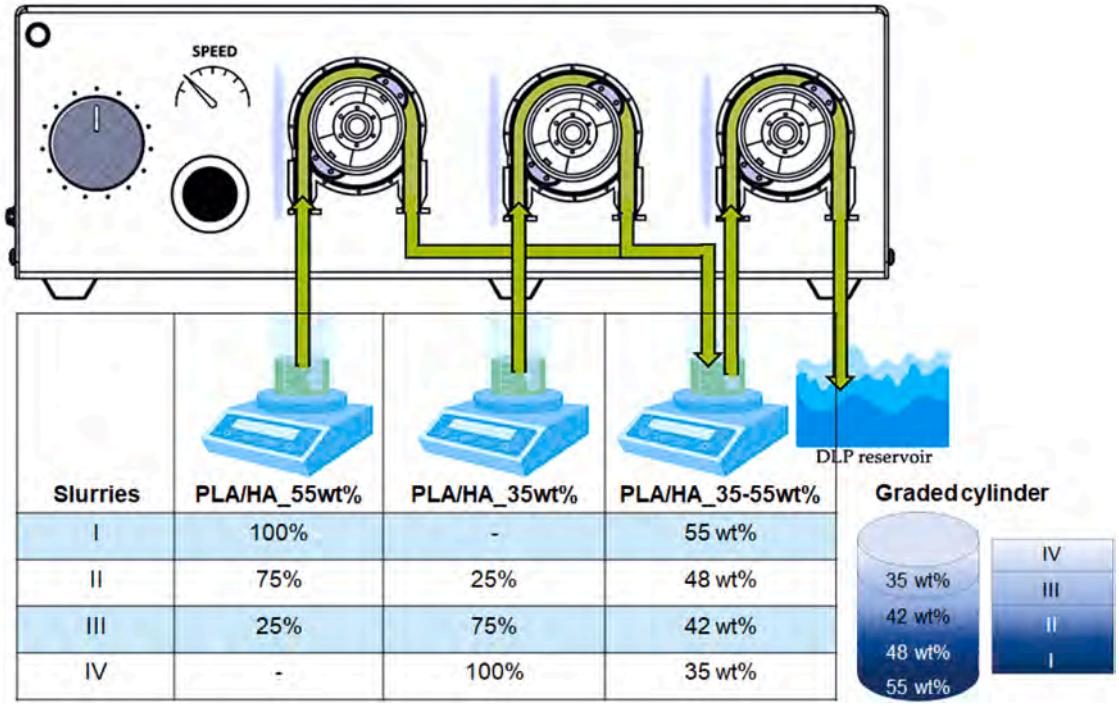


**Fig. 2.** Schematic diagram of mixing and feeding different solid loading slurries using the multi-head automatic peristaltic pump.

### 2.4. Powder, slurry and sample characterizations

The effect of ball milling on the HA particle-size distribution was investigated by laser granulometry (Mastersizer 3000, Malvern Pan'-alytical, Worcestershire, UK).

The rheological properties of the slurries were determined using a rotational rheometer (Kinexus Pro+, Netzsch Geraetebau GmbH, Selb, Germany) equipped with stainless-steel roughened parallel plates (20 mm diameter) with a 1 mm gap between plates.

The geometric densities of printed samples were determined by means of mass and geometric measurements. The densities of the specimens were also evaluated using Archimedes' method; these experimentally determined densities were compared with their theoretical values by considering the theoretical density of PLA, BYK-111 and HA, which are 1.18 g/cm$^3$, 1.06 g/cm$^3$ and 3.156 g/cm$^3$ respectively.

The phase composition was analyzed through X-ray diffraction (X'Pert PRO, Malvern Pan'alytical, Worcestershire, UK) within the 2θ range of 5–70°, employing a step size of 0.026° and an acquisition time of 5 s per step.

The thermal behavior of the photocured resin as well as of the four different regions of compositionally graded samples was determined by Thermogravimetric-Differential Thermal analyses (TG-DTA, Netzsch STA 409), performed at 10 °C/min up to 1000 °C, under static air.

The microstructure of the samples was observed by field emission scanning electron microscope (FESEM; Zeiss Supra 40, Jena, Germany) on both fractured and thermally debinded samples. The elemental composition was determined using EDX analysis. The porosity observed in the microstructure of the thermally debinded sample was quantified through imageJ software.

The compressive strength was determined using an electromechanical testing system (Zwick Roell 2014, Ulm, Germany) using a 50 kN load cell and a crosshead speed of 1 mm/min. Samples were submitted to compressive tests, under a loading direction parallel to the printing one. The tests were conducted at room temperature; at least four specimens for each formulation were subjected to mechanical tests and the average was used for interpretation.

Compressive strength was determined as the first peak following the linear elastic region of the stress-strain curve. For materials without distinct peaks, the upper yield point strength was estimated according to ISO 5833:2002, by the intersection of the stress-strain curve with a 0.2 % offset line [44]. Therefore, tests were stopped when deformation reached 25 % in all samples, not reaching complete failure.

As shown in Fig. 3, specimens were highly reproducible in terms of shape and geometrical features, as allowed by the high-resolution DLP process, as a clear advantage of the new 3D printing technologies compared to the traditional shaping methods.

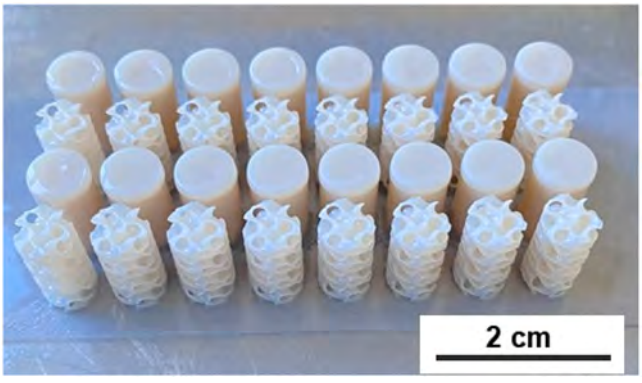


**Fig. 3.** Digital photograph of dense and gyroid-shaped cylinders, showing highly regular shapes and reproducible geometrical features.

### 2.5. Sample swelling and cytotoxicity

PLA, PLA/HA_35 wt% and PLA/HA_55 wt% uniform gyroid samples were characterized for their water up-take capacity in a physiological environment. Specifically, the sample hydration capacity in Phosphate Buffered Saline (PBS, pH 7.4) was assessed through gravimetric measurements using an analytical balance (Mettler-Toledo, XS105 Dual-Range). Each sample was weighed ($W_d$) and placed in a sterile container. PBS (10 mL/g) was then added to each sample, and the suspensions were incubated at 37 °C. After 24 h of incubation, samples were removed, wiped with filter paper to remove surface water and weighed again ($W_s$). The swelling ratio was calculated as follows:

$$Swelling\ ratio = \frac{W_s}{W_d} \tag{3}$$

where $W_s$ = swollen sample weight; $W_d$ = dry (initial) sample weight.

Dimensional variation occurring with hydration was also evaluated. Specifically, the diameter and the thickness of both the dry and hydrated samples were measured using a rheometer (MCR 301, Anton Paar). A plate-plate measuring system was employed. After setting the zero gap, the sample was placed on the lower plate. The upper plate was moved towards the lower one until a 0.2–0.4 N force was detected, indicating contact with the sample. The corresponding gap was recorded as the value for sample thickness/diameter, depending on the specific positioning of the sample on the plate.

For the swollen sample, attention was paid to maintain full hydration during the measurement. The variation in each dimension (diameter or thickness) was calculated as follows:

$$sample\ dimension\ variation\ = \frac{dimension\ of\ the\ hydrated\ sample}{dimension\ of\ the\ dry\ sample} \tag{4}$$

Experiments were carried out at least in quadruplicate and results were reported as the mean value ± standard deviation (SD). Data were statistically evaluated using one-way ANOVA tests followed by post hoc tests using Holm correction for multiple comparison. p values lower than 0.05 accounted for statistical significance.

The cytotoxicity of the samples was evaluated using an indirect test, following ISO 10993–5 guidelines with slight modifications. Briefly, the samples were washed three times with PBS and then incubated in cell culture medium at 37 °C, 5 % $CO_2$ (DMEM, 10 % FBS and 1 % P/S) (1 mL/200 mg sample) for 24 h obtaining the "conditioned medium" (cell culture medium containing potential leachable from the materials), in accordance with section 8.2 of the ISO 10993-5 standard.

Human dermal fibroblasts were seeded in a 24-well plate and cultured until around 50–60 % confluence was reached. The medium was then withdrawn and replaced with the conditioned medium from the samples. As a control, fresh culture medium was added to the cells.

After 24 h of incubation, cell morphology was observed at the light microscope and cell viability was quantified by the 3-(4,5-dimethylthiazol-2-yl)-2,5-diphenyl-2H-tetrazolium bromide (MTT) assay [45]. A Beckman DU 640 spectrophotometer (Milan, Italy) was used for absorbance measurements. Cell viability in the presence of the conditioned medium was reported as percentage, normalized to the control.

## 3. Results and discussion

### 3.1. Powder and slurry characterizations

Particle size distribution and cumulative frequency distributions of as-received and ball-milled HA powders are depicted in Fig. 4a and b, respectively, while the $D_{10}$, $D_{50}$ and $D_{90}$ values, corresponding to 10, 50 and 90 % of the cumulative distribution curves, are displayed in Fig. 4c.

As-received HA was characterized by a monomodal distribution (black curve), providing a $D_{50}$ value of 7.5 μm. After ball-milling for durations ranging from 4 to 16 h, the suspensions exhibited bimodal

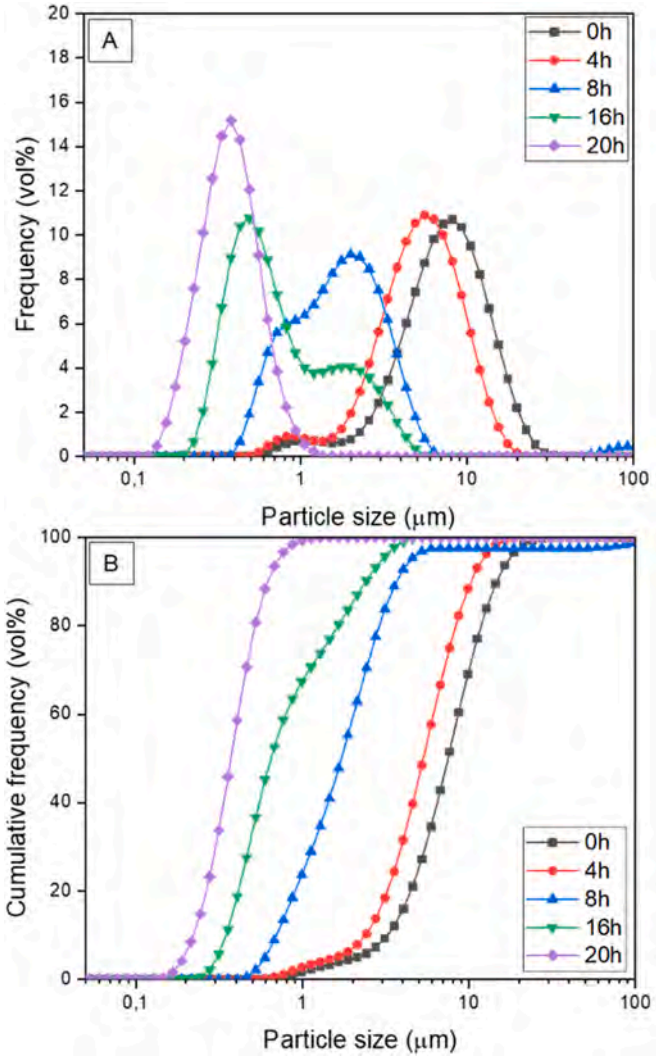


| Milling time (h) | Particle size (μm) | | |
|---|---|---|---|
| | $D_{10}$ | $D_{50}$ | $D_{90}$ |
| 0 | 3.6 | 7.5 | 16.2 |
| 4 | 2.4 | 5.3 | 10.3 |
| 8 | 0.7 | 1.7 | 3.7 |
| 16 | 0.3 | 0.6 | 2.4 |
| 20 | 0.2 | 0.38 | 0.6 |

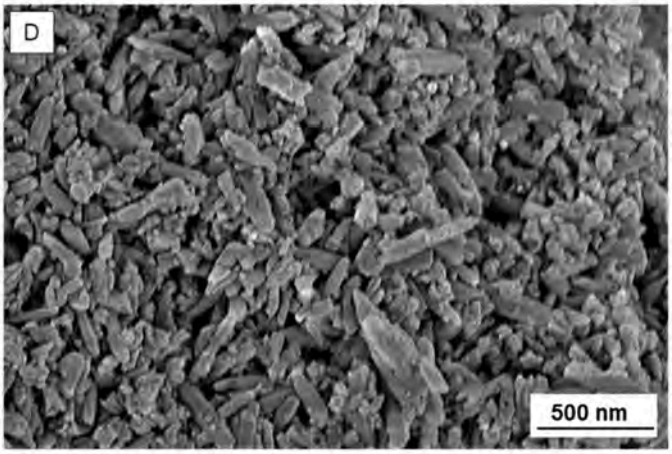


**Fig. 4.** Particle-size distribution as frequency (a) and cumulative frequency (b); $D_{10}$, $D_{50}$, $D_{90}$ values of HA powder at different ball-milling times (c). FESEM micrograph of the 20 h milled powder (d).

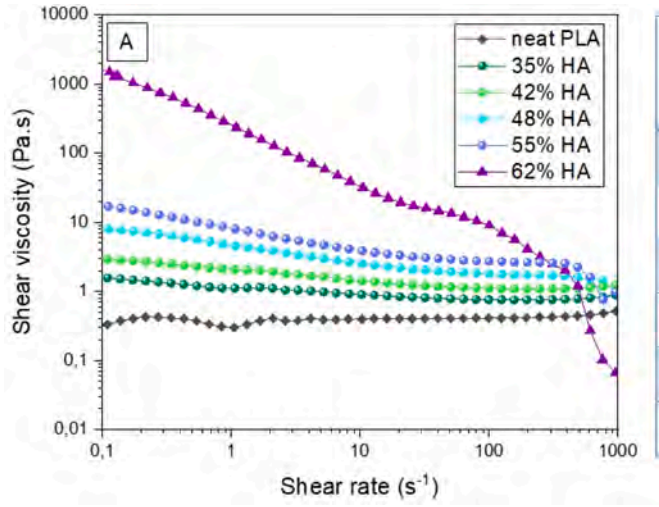


| | Dispersant amount (%) | Viscosity at 0.1 $s^{-1}$ shear rate (Pa·s) | Viscosity at 160 $s^{-1}$ shear rate (Pa·s) |
|---|---|---|---|
| PLA | 0.0 | 0.33 | 0.41 |
| PLA/HA_35wt% | 6.0 | 1.56 | 0.75 |
| PLA/HA_42wt% | 7.0 | 2.93 | 1.09 |
| PLA/HA_48wt% | 9.0 | 8.00 | 1.76 |
| PLA/HA_55wt% | 10.0 | 17.02 | 2.65 |
| PLA/HA_62wt% | 10.0 | 1485 | 5.64 |

**Fig. 5.** (a) Shear viscosity vs shear rate curves of slurries at increasing solid loadings; (b) shear viscosity values at 0.1 $s^{-1}$ and 160 $s^{-1}$ shear rates at different slurry compositions.

particle size distributions, with the intensity of the smaller-size peak progressively increasing as milling time increased.

After 20 h milling, the suspension was characterized by a narrow, monomodal distribution, with a $D_{50}$ of 0.38 μm. The cumulative distribution curves in Fig. 4b display a progressive displacement at lower sizes by increasing the milling time.

FESEM micrograph of the 20 h milled powder (Fig. 4d) showed ultrafine particles with a rod-like morphology, whose size ranged from 0.35 to 0.45 μm, in compliance with particle-size distribution determined by laser granulometry.

The rheological behavior of polymer/ceramic slurries is a key aspect for the successful fabrication of the scaffolds using DLP technique and needs to be carefully optimized. In this work, specifically, slurries at different solid contents, but all of them matching the required viscosity and printability conditions, were prepared and optimized.

In Fig. 5a, the rheological curve of the PLA liquid monomer (without HA addition) can be observed (black curve), showing an almost Newtonian behavior in the whole investigated range, as already observed in literature for neat resins and diluents suitable for stereolithography [46]. However, when HA ceramic particles are added to the liquid polymer, a slight but progressive change in the rheological behavior was observed, moving from Newtonian to shear-thinning behavior. This last behavior can be explained by considering that, at low shear rates, the agglomeration of solid particles occurs, forming complex three-dimensional networks, entrapping a certain liquid fraction. Then, as the shear rate increases, the viscosity of the slurries decreases due to the partial or complete breakdown of the agglomerates, together with the release of the trapped liquid, that decreases the friction between the particles in the flow direction [47] and provides the observed shear-thinning behavior.

The agglomeration occurring at low shear rates is promoted by the presence of ultrafine particles, as their high surface energy leads to a strong tendency to agglomerate in liquid media. In the present case, where nanometric HA powders are used, a starting agglomeration is to be expected. Indeed, a progressive increase of the starting viscosity by increasing the HA solid lading is observed, which can be attributed to greater internal friction resulting from the higher fraction of ceramic nanoparticles.

It should be noted that the behaviors shown in Fig. 5a were obtained only after careful optimization of the dispersant content, which increased from 6 wt% to 10 wt% moving from the slurry at 35 wt% HA to the one at 55 wt% HA. When the solid loading was further increased from 55 % to 62 wt% HA - while maintaining the dispersant amount fixed at 10 % to avoid excessive un-photopolymerizable organic matter - a more pronounced shear-thinning behavior was observed. Specifically, the suspension exhibited high viscosity at low shear rate, followed by a sharp but steady decrease up to approximately 150 $s^{-1}$, and then an additional significant drop at higher shear rates. In Fig. 5b, the shear viscosities at a low shear rate (0.1 $s^{-1}$ taken as a reference) and at the operative shear rate (160 $s^{-1}$) are given, as both values have to be taken into consideration for selecting the optimal slurry composition. Hinczewski et al. [46], provided an upper limit of 5 Pa·s to ensure satisfactory layer recoating, that in our system occurs at around 160 $s^{-1}$. Values in Fig. 5b show that all the slurries from 0 to 55 wt% HA satisfy this requirement, which is however slightly exceeded by the suspension at 62 wt% HA. However, this slurry exhibits a very high viscosity (≅ 1500 Pa·s) at low shear rates (i.e. 0.1 $s^{-1}$), which hinders mixing and pouring operations and reduces the effectiveness of the deairing process, increasing the risk of not complete removal of the air bubble entrapped in the slurry during the planetary mixing step. Therefore, 55 wt% solid loading was considered as the upper limit for the 3D printing specimens in this study.

Further, to assess the correct printability conditions, curing depth tests at different exposure energies were performed, as shown in Fig. 6. It is possible to observe that higher HA content leads to increased curing depth (CD) at constant exposure energy, due to enhanced light

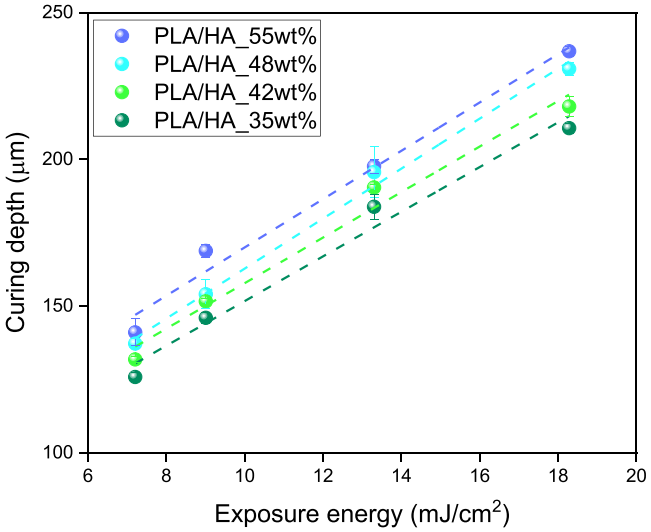


**Fig. 6.** Curing depth vs exposure energy of PLA/HA slurries at different HA contents.

scattering from a greater number of HA particles [48]. Consequently, the LED power and exposure time were adjusted (i.e. increased) for slurries with lower solid loading, compared to the PLA/HA_55wt% slurry.

Thus, the four optimized slurries (at 35 wt%, 42 wt%, 48 wt% and 55 wt% solid loading) satisfied both viscosity and printability parameters. Printing jobs were therefore carried out by using PLA, PLA/HA_35 wt% and PLA/HA_55 wt% to produce reference uniform dense cylinders and gyroids at the lowest and highest HA contents; PLA_HA_35–55 wt% was used to print compositionally graded dense and gyroid samples, as well as structurally and compositionally graded gyroid specimens.

### 3.2. *Characterization of the 3D printed samples: uniform and compositionally graded dense cylinders*

As first attempts, cylindrical samples were printed from slurries at constant amounts of 0 wt%, 35 wt% and 55 wt% HA solid loadings. Then, compositionally graded samples were printed by mixing 35 and 55 wt% HA powders slurries, as detailed in § 2.3, and schematically shown in Fig. 2. The printed samples showed a uniform shape without any deformation or warping (Fig. 7). PLA cylinder shows a translucent appearance (Fig. 7a), whereas the addition of HA renders samples opaque and white (Fig. 7b), with the degree of whiteness increasing alongside the HA content. This feature can be observed in the compositionally graded dense cylinder (Fig. 7c), particularly visible in the higher magnification image (Fig. 7d) where a color transition from less to more intense white color occurs, as the HA amount increases. The

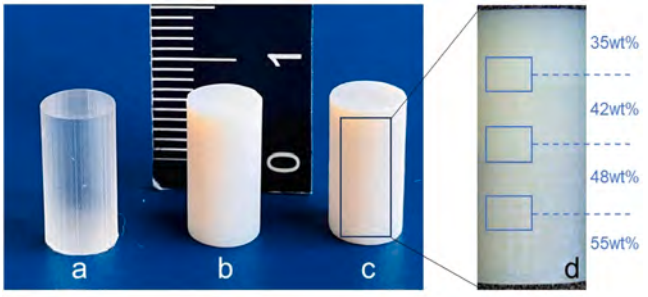


**Fig. 7.** Digital photographs of PLA_ud (a), PLA/HA_55 wt%_ud (b) and PLA/HA_35–55 wt%_gd (c). In (d) a higher magnification of PLA/HA_35–55 wt%_gd (compositionally graded dense cylinder), shows the gradual color change from the bottom to the top of the cylinder.

rectangles in Fig. 7d show the interfacial areas between different layers, showing gradual color change. Additionally, the horizontal lines resulting from layer-by-layer additive process can be observed, even if no visible delamination occurred.

Final densities were determined using both Archimedes' and geometrical measurements and compared with the theoretical density values (TD) calculated by the rule of mixtures. The data obtained has been compiled in Table 2. Considering Archimedes' densities, it is evident that neat PLA cylinder achieved the theoretical density, indicating almost no porosities and flaws in the printed samples. A slight discrepancy between the nominal and Archimedes' densities was observed for the PLA/HA composite samples, where the difference increased by increasing the HA amount. It can be reasonably assumed that an imperfect interface and low adhesion exist between the ceramic particles and the polymer matrix due to their different chemical nature. The ceramic particles are typically hydrophilic, while the polymer matrix is hydrophobic [49]. Another concurrent parameter accounting for density reduction could be reasonably imputed to the presence of air bubbles, not completely removed during the deairing step. In fact, HA addition progressively increased the slurry viscosity (see Fig. 5), making the complete air removal increasingly difficult. When Archimedes' and geometrical densities are compared, we can observe a perfect match in neat PLA samples, but some discrepancies in the PLA/HA composite specimens, with slightly higher values in the former case. As the buoyancy method implies water infiltration inside open porosities and flaws, it can result in an overestimation of the actual densities. Thus, the discrepancy between Archimedes' and geometrical densities (in the range of 1–4 %) suggests the presence of a limited number of open flaws, such as interlayer defects corresponding to the printing lines (see Fig. 7d). This discrepancy appearing only in the composites suggests an effect of the ceramic filler in contributing to the formation of flaws.

In Fig. 8, some representative FESEM micrographs of PLA/HA samples, at different magnifications, are depicted. Fig. 8a, at the lowest magnification, shows a highly compact microstructure, without large spherical pores imputable to entrapped air, contrary to the above-mentioned hypothesis and supporting the correctness of the slurry's viscosity. However, at a higher magnification (Fig. 8b), a diffused ultrafine porosity can be observed (red arrows), in compliance with the not fully density achieved by the PLA/HA composite materials. At even higher magnification (Fig. 8c), a good distribution of the HA particles, recognized by their rod-like morphology (blue arrows), embedded in the polymer matrix, can be appreciated.

FESEM analysis performed on the fracture surface of compositionally graded dense cylinder sample revealed significant insights (Fig. 9). The microstructure of the as-printed sample, depicted in Fig. 9a, exhibited high density and homogeneity, consistent with Archimedes' density values. In Fig. 9b, the microstructure of the same sample after debinding shows an increasing porosity from left to right of the micrograph (i.e., moving from the side at 55 wt% HA, to the opposite one at 35 wt% HA) due to the increasing amount of burnt-out polymer. This observation was confirmed by image analysis, demonstrating an increase in void spaces (red areas, see Fig. 9c) by decreasing the solid loading. In fact, porosity area left by polymer burn-out was observed to be 8.8 %, 10.5 %, 16.6 % and 20.7 % respectively, while moving from 55 wt% (45 % of organic matter) to 35 wt% (65 % organic matter) solid loading.

Additionally, EDX analysis were performed on the polished surface of the un-debinded sample, by moving from the right (HA: 55 wt%) to left (HA: 35 wt%) side (Fig. 10a). Although precise quantification of light elements using EDX analysis remains challenging due to limited accuracy [50], it is possible to observe a progressive variation in elemental composition. This shift is characterized by a progressive increase in the intensity of carbon peak (indicating the polymer), while the opposite behavior was observed for the P and Ca peaks (indicating hydroxyapatite) intensity (Fig. 10b).

The quantification of the HA fraction in the compositionally graded samples was carried out by DTA-TG analysis, as reported later for the compositionally and structurally graded gyroid (see Fig. 11).

The compressive stress-strain curves and elastic modulus of PLA/HA dense samples are presented in Fig. 11a and b, respectively. First, it is possible to observe that all the curves are characterized by the expected two-step behavior, with a higher slope in elastic region, followed by a slower increase in the plastic one [51]. First, the strain at yield was observed at $\cong$ 4 % for all the uniform and compositionally graded dense cylinders. Second, by observing the results of the two reference materials, PLA/HA_35 wt% achieved higher yield strength and elastic modulus compared to PLA/HA_55 wt%. The decrease of mechanical properties, by increasing the HA amount, has been already reported in literature, both under tensile [52] and compressive stress [53–55], and has been attributed to different reasons, such as a poor dispersion of HA particles in PLA as well as to weak interface between the ceramic filler and polymer matrix [56,57]. In addition, when 3D printing techniques are used, additional challenges arise by the presence of HA particles inducing nozzle closing (in extrusion-based methods) or slurry viscosity increase and layer curability decrease (in vat-photopolymerization methods). In this study, FESEM observation showed an even dispersion of the HA particles in the polymer matrix, while rheological studies indicated that – even at 55 wt% HA loading, the viscosity was still suitable for successful printing. Thus, the observed decrease of mechanical properties can be reasonably associated to the poor compatibility between hydrophobic PLA and hydrophilic calcium phosphates. In the attempt to overcome this issue, the surface functionalization of HA with silane [58], lactic acid [59], or fatty acids [60] are currently under investigation, showing good degree of success in terms of compatibility with PLA. In spite of its importance, this aspect has not been considered here and will be the focus of future work. Here, it is relevant to observe that the compositionally graded scaffold (PLA/HA_35–55 wt%_*gd*) shows mechanical properties that fall within the range observed for PLA/HA_35 wt%_*ud* and PLA/HA_55 wt%_*ud* specimens up to the yield point. A linear correlation between elastic modulus and HA content was determined when the HA fraction of the compositionally graded sample was averaged to 45 wt%, as shown in Fig. 11b. These results strengthen the capability of the process to modulate the HA content and to tune it at the expected values.

The compressive stress at yield, toughness and elastic modulus values of uniform and compositionally graded cylinders are collected in Table 3.

**Table 2**
Theoretical and experimental densities determined by geometrical and Archimedes' methods of uniform and compositionally graded dense cylinders.

| Sample Name | Theoretical Density g/cm$^3$ | Archimedes' Density g/cm$^3$ (% TD) | Geometrical Density g/cm$^3$ (% TD) |
|---|---|---|---|
| **PLA_*ud*** | 1.18 | 1.18 ± 0.01 (99.9 %) | 1.18 ± 0.01 (99.9 %) |
| **PLA/HA_35 wt %_*ud*** | 1.51 | 1.49 ± 0.01 (99.3 %) | 1.43 ± 0.02 (94.7 %) |
| **PLA/HA_35–55 wt%_*gd*** | 1.65 | 1.62 ± 0.02 (98.6 %) | 1.60 ± 0.03 (97.0 %) |
| **PLA/HA_55 wt %_*ud*** | 1.79 | 1.74 ± 0.01 (97.6 %) | 1.67 ± 0.01 (93.3 %) |

### 3.3. *Characterization of the 3D printed samples: uniform and compositionally graded gyroids*

In Fig. 12, some representative digital photographs of the uniform and compositionally graded gyroid samples are depicted. It is possible to observe the high precision and accuracy of the DLP process to reproduce the architectural features of the designs. It is important to note that previous studies on PLA/HA scaffolds fabricated by 3D printing predominantly identified Fused Deposition Modelling (FDM) as the

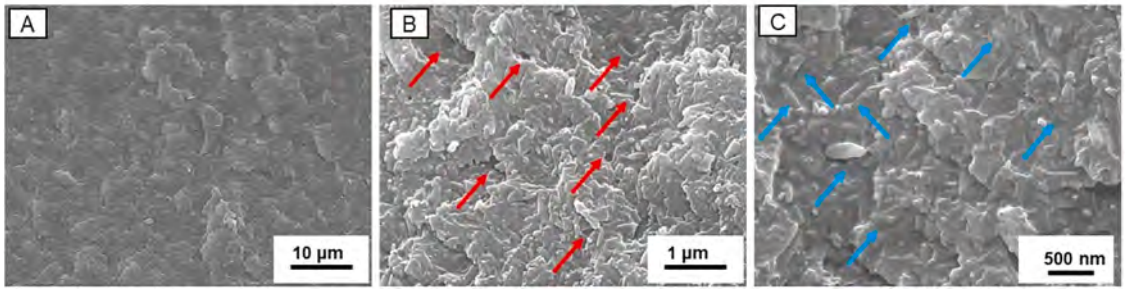


**Fig. 8.** FESEM micrographs of PLA/HA samples at different magnifications (red arrows indicate porosity; blue arrows indicate HA particles).

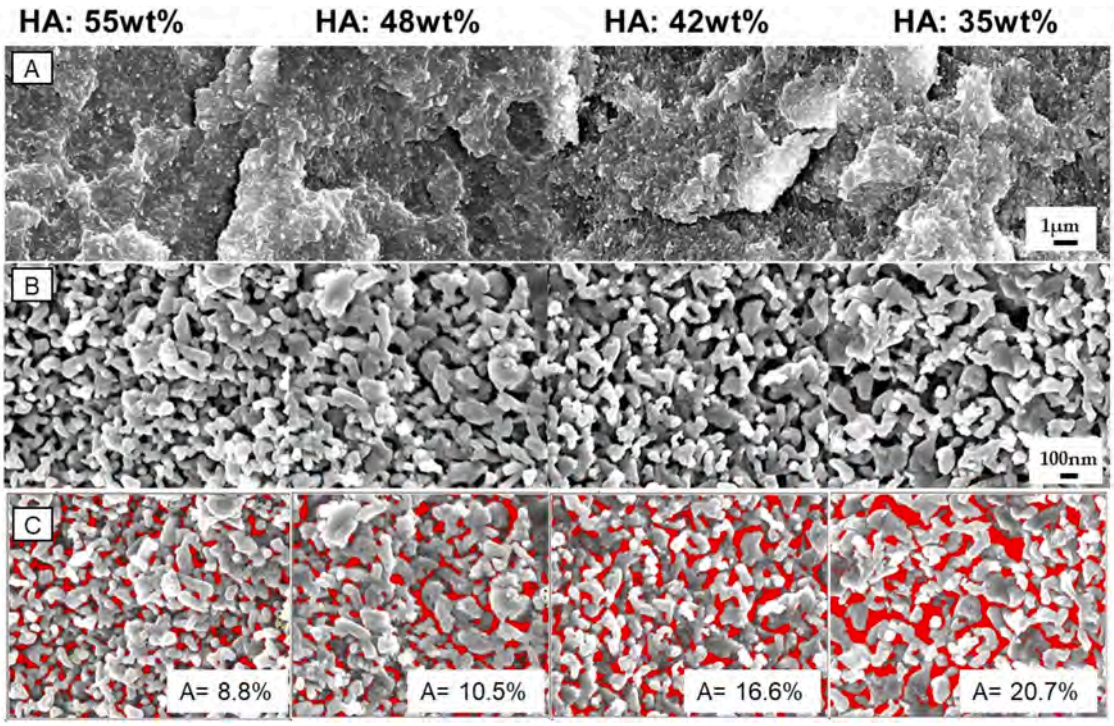


**Fig. 9.** FESEM micrographs of the compositionally graded dense sample (PLA/HA35–55 wt%_gd) from lower (left side) to higher (right side) HA solid loading: as-printed (a); thermally debinded sample showing increasing porosity due to the polymer burn-out (b); thermally debinded sample where the porosity areas are highlighted in red and quantified by image J analysis (c).

preferred technology [57,61–71] owing to its simplicity and low cost [61] for processing thermoplastic polymer-based materials. However, in most cases, the scaffolds were designed as 'simple' lattice structures rather than triply periodic minimal surfaces (TPMS), likely due to the more limited control over internal architectural features achievable with FDM compared to vat photopolymerization techniques.

Furthermore, achieving compositional gradation, particularly within a single processing step, represents a significant and innovative advancement. Only a few previous examples can be cited. For instance, Wang et al. [62] fabricated bilayer scaffolds for osteochondral defect repair using FDM technology by sequentially depositing thermoplastic polyurethane and a PLA/HA composite to form the cartilage and bone layers, respectively. This process required switching the heating cylinder and adjusting the nozzle temperature for each layer, followed by post-impregnation of the cartilage layer with a gelatin/sodium alginate mixture to create a microenvironment conducive to cell proliferation. Similarly, Thunsiri et al. [70] developed bilayer scaffolds for articular cartilage repair using FDM, where a polycaprolactone (PCL)/PLA/L/HA layer overlaid with a PLA/PCL layer. Post-impregnation of the upper layer with a chitosan/silk solution and subsequent freeze-drying were necessary to achieve a porous, spongy structure. Liu et al. [71] fabricated TPMS scaffolds from pure PLA and achieved a compositional gradient through successive post-impregnation steps using PLA/HA mixtures with varying HA concentrations (5 to 30 wt%). After six impregnation cycles, layers at increasing HA content from the inner PLA core to the outer HA-enriched surface were obtained. Despite these efforts, these approaches involved multiple processing steps and resulted only in discrete, rather than continuous, compositional gradients.

Experimental densities of uniform and compositionally graded gyroid were determined using Archimedes' principle and compared to the corresponding theoretical values delineated in Table 4. As it is already investigated in dense samples, the achievement of the theoretical density in the dense gyroid made by neat PLA can be appreciated; then, a certain discrepancy between the nominal and Archimedes' densities were observed in PLA/HA composite gyroid samples, attributed to imperfect interfaces and weak adhesion between the ceramic particles and the polymer matrix, as previously discussed. Porosity levels in all gyroid structures were estimated to be approximately 80 %, aligning with the design density of 20 % as per the MS Lattice model.

The compressive strength curves and elastic modulus of uniform and compositionally graded gyroid samples are presented in Fig. 13a and b, respectively. In line with the results of the dense samples, the highest

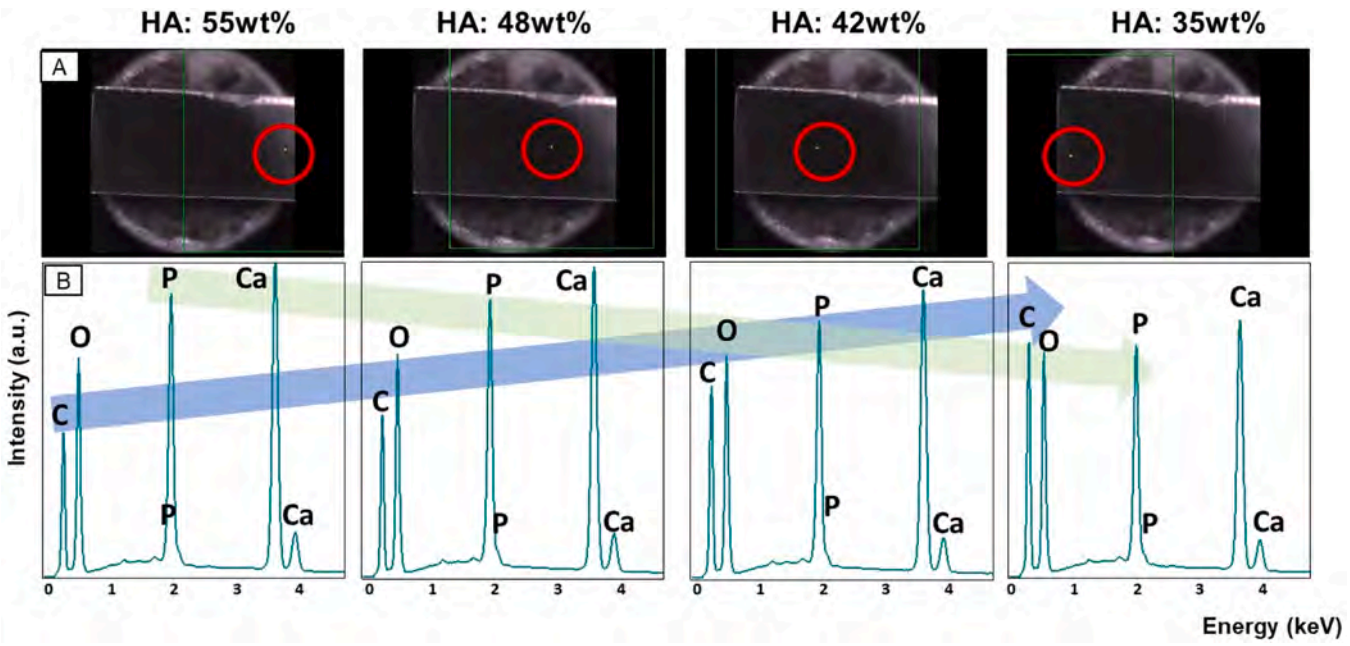


**Fig. 10.** EDX analysis on selected areas of the compositionally graded sample, from the left side to right one. (a): Low magnification images showing the analyzed areas; (b): EDX elemental plots.

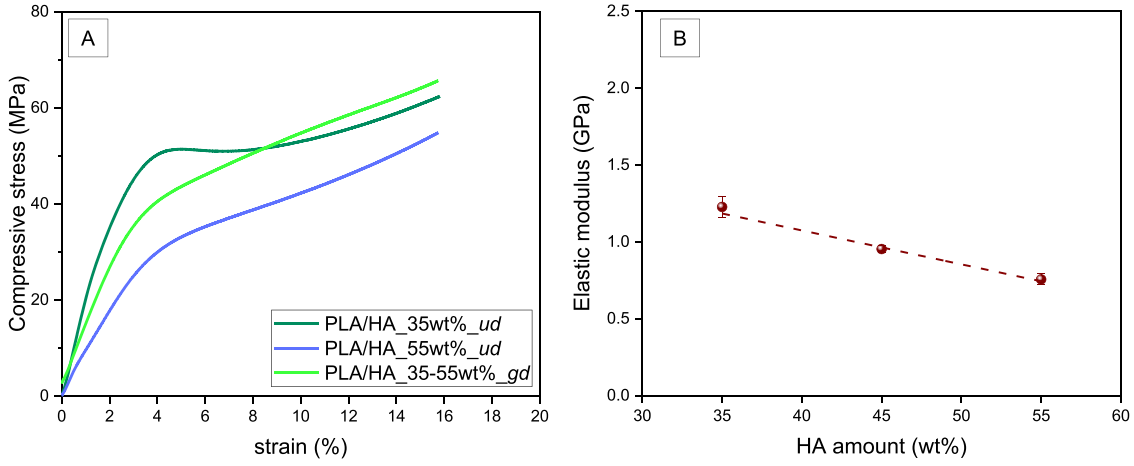


**Fig. 11.** Compressive stress-strain curves (a) and elastic modulus (b) of uniform and compositionally graded dense cylinders.

**Table 3**
Compressive stress at yield, toughness and elastic modulus of uniform and compositionally graded dense cylinders.

| Sample Name | Compressive stress at yield (MPa) | Toughness ($Jm^{-3}$) | Elastic Modulus (GPa) |
|---|---|---|---|
| **PLA/HA_35 wt% _ud** | 49.7 ± 0.2 | 8.3 ± 0.1 | 1.23 ± 0.07 |
| **PLA/HA_35–55 wt%_gd** | 40.9 ± 0.3 | 7.4 ± 0.1 | 0.98 ± 0.03 |
| **PLA/HA_55 wt% _ud** | 31.5 ± 0.2 | 6.2 ± 0.2 | 0.75 ± 0.04 |

mechanical properties were achieved for the samples at 35 wt% HA, whereas excess hydroxyapatite content, as in PLA/HA_55 wt%_*ug*, led to a decrease of both compressive yield strength and elastic modulus. However, it is important to note that, once again, the compressive curve of compositionally graded material, with a progressive increasing HA concentration from 35 wt% to 55 wt%, falls between the two reference samples.

The mechanical properties achieved by the gyroid samples were more than one order of magnification lower than corresponding dense samples, according to previous studies comparing dense and porous structures [72].

The very high degree of porosity (in the range 82–85 %) does not account for such a decrease of mechanical properties, and a simple relationship between compressive yield strength (or elastic modulus) and porosity does not provide a realistic model in these materials. In dense structures, compressive strength and stiffness are due to their continuous, solid architecture, which efficiently distributes applied loads. In contrast, TPMS based gyroid structures, characterized by their interconnected porous networks and curved surfaces, experience stress concentrations at the nodes and struts, according to the Gibson and Ashby theory for cellular solids [72,73], leading to mechanical properties not only ascribable to the amount of porosity present, but to the geometric features themselves.

In particular, wall thickness and cells number play a pivotal role in the mechanical properties since both contribute to relative density

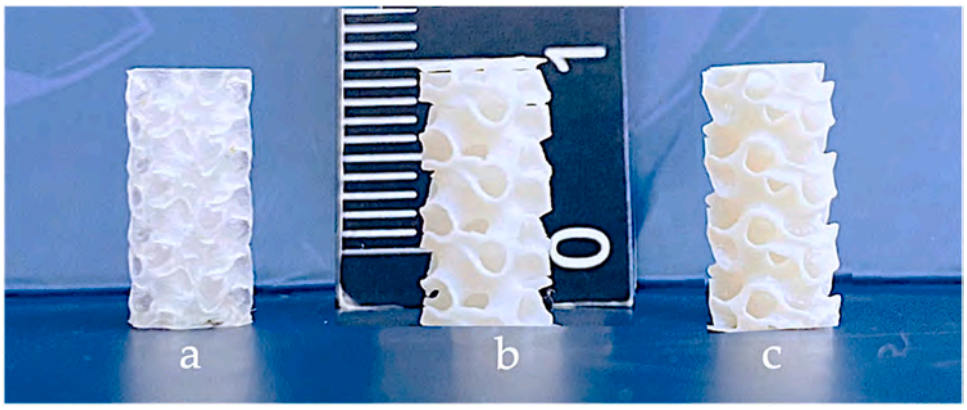


**Fig. 12.** Photograph of PLA_ug (a); PLA/HA_55 wt%_ug (b); Compositionally graded PLA/HA_35–55 wt%_gg (c) gyroid samples.

**Table 4**
Theoretical, experimental densities and porosity determined by Archimedes' method of uniform and compositionally graded gyroid structures.

| Sample Name | Theoretical Density (g/cm$^3$) | Archimedes' Density (g/cm$^3$) (%TD) | Scaffold Porosity (%) |
|---|---|---|---|
| **PLA_*ug*** | 1.18 | 1.18 ± 0.02 (99.6 %) | 78.8 ± 1.0 |
| **PLA/HA_35 wt %_*ug*** | 1.51 | 1.47 ± 0.03 (97.3 %) | 81.7 ± 1.5 |
| **PLA/HA_35–55 wt%_*gg*** | 1.65 | 1.61 ± 0.03 (97.8 %) | 82.6 ± 0.5 |
| **PLA/HA_55 wt %_*ug*** | 1.79 | 1.71 ± 0.02 (95.5 %) | 84.7 ± 0.4 |

calculation [74,75]. In this study, we investigated relative densities ranging between 15–20 % (Table 5), resulting from the very thin walls thickness of the designed gyroid (about 300 μm). Maconachie et al. [74] found a lower limit of 500 μm for wall thickness to have consistent compressive results while 300 μm samples reported a significantly lower modulus than all other specimens, for ABS gyroid geometries prepared via Fused Deposition Modeling (FDM).

The key point in this work is to show how mechanical properties can vary, in a single scaffold, from one layer to the opposite one.

### 3.3.1. *Samples swelling in physiological medium and cytotoxicity*

Results on swelling behavior in PBS of PLA_*ug*, PLA/HA_35 wt%_*ug* and PLA/HA_55 wt%_*ug* are depicted in Fig. 14(a). When equilibrated in PBS, PLA showed a swelling ratio (SR) of 2.1 that increased to around 2.4 in the PLA/HA samples, showing significantly higher water up-take in the composites compared to neat polymer. This is consistent with the hydrophilic nature of HA and with literature data reporting higher swelling extent for composite materials containing inorganic hydrophilic filler combined to polyester-based networks in respect to the neat organic matrix [76,77].

As for the sample dimensional variation accompanying swelling, depicted in Fig. 14(b), PLA samples exhibited no significant variation in either thickness and diameter after equilibration in physiological medium. In contrast, PLA/HA composites exhibited a measurable thickness increase of approximately 3 % when swollen in PBS.

These data can be rationally explained considering the hydrophobic nature of the PLA sample whose water up-take could be primarily attributed to the filling of the sample's void volume with PBS while, in the presence of HA, a true hydration of the matrix also occurs leading to a slight swelling in dimension.

The opposite nature of the hydrophobic polymer and hydrophilic ceramic filler well explains the relationship between the HA content and

**Table 5**
Compressive stress at yield, toughness and elastic modulus of gyroid samples.

| Sample Name | Compressive stress at yield (MPa) | Toughness (Jm$^{-3}$) | Elastic Modulus (MPa) |
|---|---|---|---|
| **PLA/HA_35 wt% _*ug*** | 1.80 ± 0.06 | 0.15 ± 0.01 | 39.5 ± 1.4 |
| **PLA/HA_35–55 wt%_*gg*** | 1.13 ± 0.01 | 0.09 ± 0.01 | 14.7 ± 2.0 |
| **PLA/HA_55 wt% _*ug*** | 0.63 ± 0.05 | 0.07 ± 0.01 | 10.0 ± 1.0 |

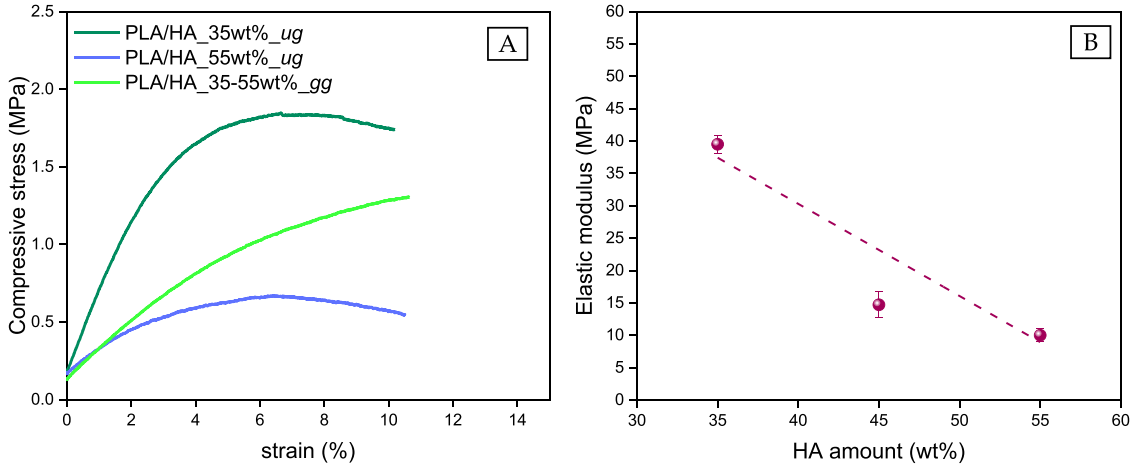


**Fig. 13.** Compressive stress-strain curves (a) and elastic modulus (b) of uniform gyroid samples.

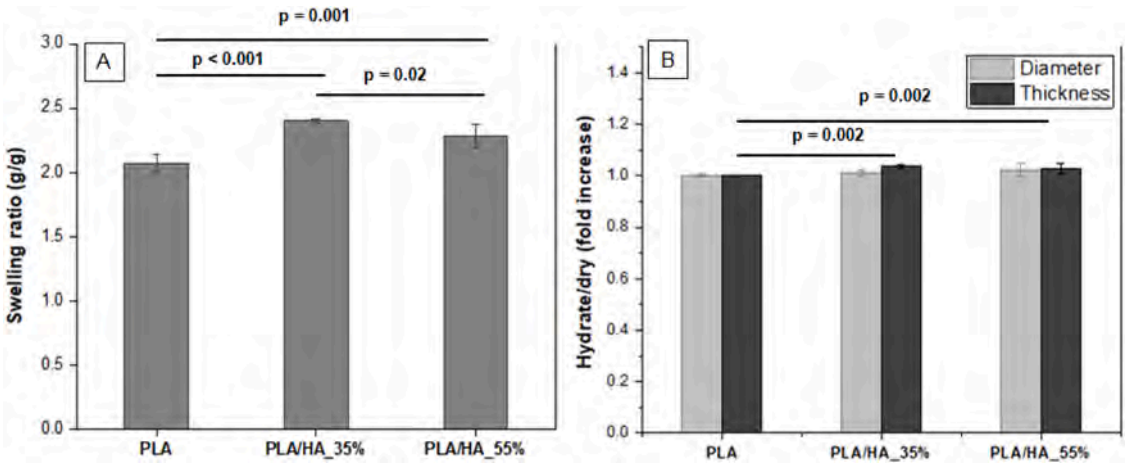


**Fig. 14.** Sample hydration behavior at equilibrium in PBS at 37 °C for PLA_*ug*, PLA/HA_35 wt%_ug and PLA/HA_55 wt%_*ug*: a) swelling ratio and b) dimensional change for the diameter and thickness.

the mechanical properties observed for both dense and gyroid samples, described in the previous sections. While the composite formulation will be further optimized in the future in view of application towards targeted tissue, it is important to note that the higher water up-take observed in HA-containing materials, providing a more hydrated environment for cells, is expected to have a positive impact on material-cell interaction.

As for the cytotoxicity studies, optical micrographies of HDF, at $t$ = 0 and after 24 h of incubation with cell culture medium conditioned with PLA/HA_55 wt%_*ug* sample, are depicted in Fig. 15. Images of the same cells incubated with fresh cell culture medium (ctr) are reported as well. Images clearly indicated that cells incubated with the conditioned medium retained their typical morphology thus suggesting that no toxic leachable components was released from the tested samples. This was confirmed by quantitative MTT data indicating that cell viability in the presence of the conditioned medium was comparable (110 ± 12 %) to the one recorded for the control.

Even if a complete biological characterization is out of the scope of this work, these results demonstrated that no adverse effects from (possible) residual uncured monomers, photo-initiator and/or dispersant occurred, demonstrating the suitability of the formulation and the printing process for tissue engineering purpose.

### 3.4. *Characterization of the 3D printed samples: compositionally and structurally graded gyroids*

The digital photograph of a gyroid sample characterized by both compositional and structural gradients (PLA/HA_35–55 wt%_sgg) is shown in Fig. 16. Besides the frontal picture (Fig. 16a), images of the upper and lower surfaces are depicted as well (Fig. 16b-c), to highlight

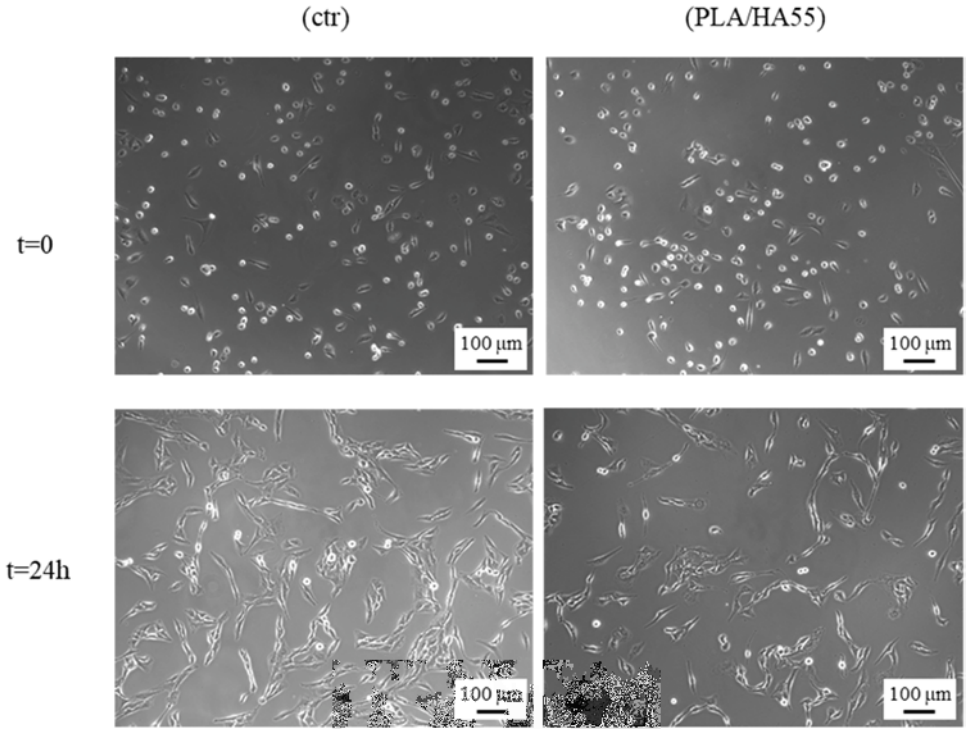


**Fig. 15.** Images (obtained at the optical microscope) of HDF incubated with fresh cell culture medium (ctr) and with cell culture medium, previously conditioned with PLA/HA_55 wt%_*ug*, at $t$ = 0 and after 24 h of incubation.

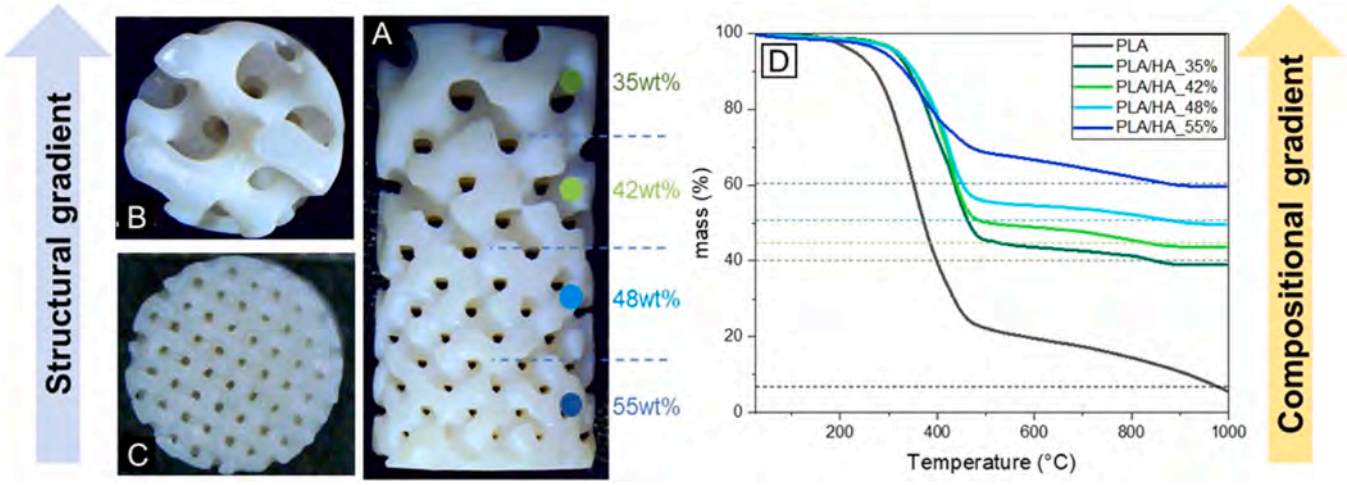


**Fig. 16.** Digital photograph of the structurally and compositionally graded gyroid (PLA/HA_35–55 wt%_sgg) (a), showing the upper (b) and lower (c) surfaces to highlight the structural gradient.

the structural gradient and architectural features within the sample. Colored points in (Fig. 16a) are associated to material sampling and analysis by thermogravimetric analysis, shown in (Fig. 16d), used to quantify the effective HA content in four different sections of each specimen. As a reference, the thermogravimetric curve of neat PLA is reported as well, showing a not complete decomposition of the photocured polymer at 1000 °C, providing a residual mass of 5.7 %, in good agreement with previous literature reporting the thermal decomposition of polylactide fibers [78] or other photocured crosslinked polymers [79]. Considering the PLA residual mass in each composition, the samples at 35 wt%, 42 wt%, 48 wt% and 55 wt% HA provided the residual mass of 35.3 wt%, 40.3 wt%, 46.6 wt% and 56.8 wt%, in a close agreement with the nominal ones, with errors ranging between 0.8 and 4.2 %.

The enormous potential of DLP, in simultaneously controlling the compositional and structural variation into complex structures using PLA/HA composite slurries, presents an innovative paradigm for the customization of scaffolds on any type of complex and multi-layered scaffolds. In contrast to conventional techniques [80–82] that frequently encounter challenges in regulating both compositional and structural gradients within intricate scaffolds, DLP enable precise control over these parameters. Such a degree of customization is crucial for tailoring scaffolds to specific biological, structural and mechanical requirements, ensuring optimal tissue regeneration and functional efficacy. The ability to engineer multi-layered scaffolds with diverse properties further enhances the adaptability and potential of this technique, thereby paving the way for advanced tissue engineering applications.

The future goal will be to exploit this approach for the fabrication of scaffolds specifically designed for the regeneration of complex human tissues, like the osteochondral one. Scaffolds matching the features of cartilage tissue (on one side) and of bone (on the other) will be properly designed on the ground of porosity, permeability, and biomechanical properties of the two tissues, and their intermediate layers. Fluid dynamic simulations will support the design of the complex scaffolds, allowing to optimize the architectural features on the ground of (for instance) permeability requirements [83]. The results of the cytotoxicity tests, carried out according to ISO 10993–5 guidelines, suggest scaffolds' biocompatibility. However, these tests represent only an initial, albeit mandatory, step in evaluating the scaffolds' potential for tissue engineering applications. More comprehensive studies, also using more specific cell lines, are certainly needed to fully assess their suitability. In this regard, ongoing experiments aim to evaluate the response of human mesenchymal stromal cells to the scaffolds, particularly regarding their ability to promote cell adhesion, proliferation, and differentiation. Micro and nanomechanical tests (such as nanoindentation, atomic force microscope and FESEM coupled with in-situ nanoindentation) will be useful to provide not only the macroscopic and global mechanical behavior of the scaffold but also local properties and their variation within the structure, to prove the matching of specific scaffold parts to the different human tissues.

## 4. Conclusions and future perspectives

In this work, vat photopolymerization of PLA/HA composites is proposed to fabricate graded scaffolds in terms of composition and structure for osteochondral or other "interface tissues" regeneration applications. First, uniform dense and gyroid-shaped cylinders were printed using the optimized PLA/HA composite slurries with constant solid loading 35 wt% and 55 wt% with compatible viscosity and high controllability. Then, compositionally graded samples were successfully printed using a controlled multi-head automatic peristaltic pump to develop a continuous compositional gradient, by mixing both slurries. The resulting high-precision uniform and compositionally graded samples were obtained without deformation and delamination between the printing layers. The compositionally graded sample exhibited high density and homogeneity throughout, with a gradual increase in HA content from bottom to top. It has been shown that the HA filler amount has to be properly optimized to maximize the compressive yield strength of dense cylinder structures, with the compositionally graded sample showing mechanical properties intermediate between those of the lowest and highest HA content samples.

Furthermore, structurally and compositionally graded samples were also successfully printed, demonstrating – for the first time with the vat-photopolymerization technique – the feasibility to obtain both gradients in a single printing job. Preliminary studies of sample behavior in physiological environment excluded the risk of cytotoxicity due to formulations (such as residual monomers, photo-initiator, dispersant) and supported the potential use of the developed materials for tissue engineering purposes.

In future work, this approach will be further developed to fabricate advanced scaffolds that mimic the intricate physio-chemical, biomechanical and structural characteristics of specific complex tissues like osteochondral interfaces. These scaffolds will be accurately engineered to match the porosity, permeability, and biomechanics of both cartilage and bone, including intermediate transitional layers, while ensuring a smooth and continuous gradient in both composition and structure. The design process will be supported by computational fluid dynamics (CFD)

simulations, which will guide the optimization of architectural features based on specific parameters such as permeability requirements.

Ongoing research is demonstrating the feasibility of modifying neat PLA not only with calcium phosphate particles, but also with natural biopolymers, such as gelatin, still achieving correct slurry viscosity and printability. Incorporating natural polymers is expected to improve cellular behavior and differentiation—particularly toward chondrogenic and osteogenic lineages—while also better mimicking the low-modulus mechanical behavior of tissues like surface articular cartilage.

Improvements to the physical and mechanical characterisation of the scaffolds will also be pursued. To this extent, techniques such as nano-indentation, atomic force microscopy (AFM), and field-emission scanning electron microscopy (FESEM) combined with in-situ mechanical testing will be employed. These methods will not only provide insights into the global mechanical performance of the scaffold but also reveal localized variations in mechanical properties across different scaffold regions—critical for verifying the functional alignment of each region with its corresponding native tissue. Full biological characterization will include the evaluation of human mesenchymal stromal cell response to the scaffolds, with particular attention to the ability of the different scaffold regions to support cells adhesion, proliferation, and differentiation toward chondrogenic and osteogenic lineages.

This tissue-targeted design strategy holds the potential to significantly advance the field of regenerative implants by enabling seamless integration with the surrounding native complex tissues, thus enhancing implant functionality and clinical outcomes.

## CRediT authorship contribution statement

**Zahid Abbas:** Writing – original draft, Validation, Methodology, Investigation, Formal analysis, Data curation. **Jeevankumar Pallagani:** Writing – review & editing, Software, Methodology, Investigation, Formal analysis, Data curation. **Annalisa La Gatta:** Writing – review & editing, Supervision, Resources, Investigation, Funding acquisition, Formal analysis, Data curation. **Chiara Schiraldi:** Writing – review & editing, Validation, Supervision, Investigation, Data curation. **Paola Palmero:** Writing – review & editing, Writing – original draft, Supervision, Resources, Project administration, Methodology, Investigation, Funding acquisition, Formal analysis, Data curation. **Bartolomeo Coppola:** Writing – review & editing, Writing – original draft, Validation, Supervision, Methodology, Investigation, Data curation.

## Declaration of competing interest

The authors declare the following financial interests/personal relationships which may be considered as potential competing interests:

Paola Palmero reports financial support was provided by Italian Ministry of University and Research (MUR). Bartolomeo Coppola reports financial support was provided by European Union. If there are other authors, they declare that they have no known competing financial interests or personal relationships that could have appeared to influence the work reported in this paper.

## Acknowledgements

We acknowledge financial support under the National Recovery and Resilience Plan (NRRP), Mission 4, Component 2, Investment 1.1, Call for tender No. 104 published on 2.2.2022 by the Italian Ministry of University and Research (MUR), funded by the European Union – NextGenerationEU – Project 20228JPCTY - Title - DEsign and Stereolithography of cell-Instructive gradient scaffolds for osteochondral tissue REgeneration (DESIRE) – CUP E53D23005180006 - Grant Assignment Decree No. 966 adopted on 30–06–2023 by the Italian Ministry of Ministry of University and Research (MUR).

This study was carried out within the MICS (Made in Italy – Circular and Sustainable) Extended Partnership and received funding from the European Union Next-GenerationEU (PIANO NAZIONALE DI RIPRESA E RESILIENZA (PNRR) – MISSIONE 4 COMPONENTE 2, INVESTIMENTO 1.3 – D.D. 1551.11–10–2022, PE00000004). This manuscript reflects only the authors' views and opinions, neither the European Union nor the European Commission can be considered responsible for them.

## Data availability

Data will be made available on request.

## References

[1] Y. Han, H. Lei, H. Kaken, W. Zhao, W. Wang, A. Wumanerjiang, W. Peng, L. Guo, L. Gu, Q. Kong, 3D printing customized design of human bone tissue implant and its application, Nanotechnol. Rev. 11 (2022) 1792–1801.

[2] K.C. Wong, 3D-printed patient-specific applications in orthopedics, Orthop. Res. Rev. (2016) 57–66.

[3] R. Baptista, M. Guedes, M.F.C. Pereira, A. Mauricio, H. Carrelo, T. Cidade, On the effect of design and fabrication parameters on mechanical performance of 3D printed PLA scaffolds, Bioprinting 20 (2020) e00096.

[4] C.O. Flynn, B.A.O. McCormack, A three-layer model of skin and its application in simulating wrinkling, Comput. Methods Biomech. Biomed. Eng. 12 (2009) 125–134.

[5] A. Seidi, M. Ramalingam, I. Elloumi-Hannachi, S. Ostrovidov, A. Khademhosseini, Gradient biomaterials for soft-to-hard interface tissue engineering, Acta Biomater. 7 (2011) 1441–1451.

[6] B. Vigani, D. Ianev, M. Adami, C. Valentino, M. Ruggeri, C. Boselli, A. Icaro Cornaglia, G. Sandri, S. Rossi, Porous functionally graded scaffold prepared by a single-step freeze-drying process. A bioinspired approach for wound care, Int. J. Pharm. 656 (2024) 124119, https://doi.org/10.1016/j.ijpharm.2024.124119.

[7] L. Chen, L. Wei, X. Su, L. Qin, Z. Xu, X. Huang, H. Chen, N. Hu, Preparation and characterization of biomimetic functional scaffold with gradient structure for osteochondral defect repair, Bioengineering 10 (2023) 213.

[8] S. Micalizzi, L. Russo, C. Giacomelli, F. Montemurro, C. De Maria, M. Nencioni, L. Marchetti, M.L. Trincavelli, G. Vozzi, Multimaterial and multiscale scaffold for engineering enthesis organ, Int. J. Bioprint 9 (2023).

[9] K. Kalia, A. Ameli, Additive manufacturing of functionally graded foams: material extrusion process design, part design, and mechanical testing, Addit. Manuf. 79 (2024) 103945.

[10] L. Ren, Z. Wang, L. Ren, Z. Han, Q. Liu, Z. Song, Graded biological materials and additive manufacturing technologies for producing bioinspired graded materials: an overview, Compos. B Eng. 242 (2022) 110086.

[11] F. Corrado, L. Di Maio, P. Palmero, B. Coppola, Z. Abbas, A. La Gatta, C. Schiraldi, P. Scarfato, Vat photo-polymerization 3D printing of gradient scaffolds for osteochondral tissue regeneration, Acta Biomater. 200 (2025), https://doi.org/10.1016/j.actbio.2025.05.042.

[12] A. Tampieri, M. Sandri, E. Landi, D. Pressato, S. Francioli, R. Quarto, I. Martin, Design of graded biomimetic osteochondral composite scaffolds, Biomaterials 29 (2008) 3539–3546.

[13] E. Amann, A. Amirall, A.R. Franco, P.S.P. Poh, F.J. Sola Dueñas, G. Fuentes Estévez, I.B. Leonor, R.L. Reis, M. van Griensven, E.R. Balmayor, A graded, porous composite of natural biopolymers and octacalcium phosphate guides osteochondral differentiation of stem cells, Adv. Healthc. Mater. 10 (2021) 2001692.

[14] C. Zhen, Y. Shi, W. Wang, G. Zhou, H. Li, G. Lin, F. Wang, B. Tang, X. Li, Advancements in gradient bone scaffolds: enhancing bone regeneration in the treatment of various bone disorders, Biofabrication 16 (2024) 032004.

[15] C. Petit, J.-M. Tulliani, S. Tadier, S. Meille, J. Chevalier, P. Palmero, Novel calcium phosphate/PCL graded samples: design and development in view of biomedical applications, Mater. Sci. Eng.: C 97 (2019) 336–346.

[16] J.M. Lowen, J.K. Leach, Functionally graded biomaterials for use as model systems and replacement tissues, Adv. Funct. Mater. 30 (2020) 1909089.

[17] A. Di Luca, I. Lorenzo-Moldero, C. Mota, A. Lepedda, D. Auhl, C. Van Blitterswijk, L. Moroni, Tuning cell differentiation into a 3D scaffold presenting a pore shape gradient for osteochondral regeneration, Adv. Healthc. Mater. 5 (2016) 1753–1763.

[18] X. Dong, H. Zhao, J. Li, Y. Tian, H. Zeng, M.A. Ramos, T.S. Hu, Q. Xu, Progress in bioinspired dry and wet gradient materials from design principles to engineering applications, IScience 23 (2020).

[19] A.P.G. Castro, T. Pires, J.E. Santos, B.P. Gouveia, P.R. Fernandes, Permeability versus design in TPMS scaffolds, Materials 12 (2019) 1313.

[20] X. Wu, Q. Lian, D. Li, Z. Jin, Biphasic osteochondral scaffold fabrication using multi-material mask projection stereolithography, Rapid Prototyp. J. 25 (2019) 277–288.

[21] S. Liu, S. Qin, M. He, D. Zhou, Q. Qin, H. Wang, Current applications of poly (lactic acid) composites in tissue engineering and drug delivery, Compos. B Eng. 199 (2020) 108238.

[22] N. Shekhar, A. Mondal, Synthesis, properties, environmental degradation, processing, and applications of polylactic acid (PLA): an overview, Polym. Bull. (2024) 1–37.

[23] N.G. Khouri, J.O. Bahú, C. Blanco-Llamero, P. Severino, V.O.C. Concha, E.B. Souto, Polylactic acid (PLA): properties, synthesis, and biomedical applications-a review of the literature, J. Mol. Struct. (2024) 138243.

[24] I. Vindokurov, Y. Pirogova, M. Tashkinov, V.V. Silberschmidt, Compression of additively manufactured PLA for biomedical applications: effects of test conditions on properties of solid samples, Polym. Test. 130 (2024) 108320.
[25] G. Lehmann, P. Palmero, I. Cacciotti, R. Pecci, L. Campagnolo, R. Bedini, G. Siracusa, A. Bianco, A. Camaioni, L. Montanaro, Design, production and biocompatibility of nanostructured porous HAp and Si-HAp ceramics as three-dimensional scaffolds for stem cell culture and differentiation, Ceram.-Silikaty 54 (2010) 90–96.
[26] M. Karimi, A. Asefnejad, D. Aflaki, A. Surendar, H. Baharifar, S. Saber-Samandari, A. Khandan, A. Khan, D. Toghraie, Fabrication of shapeless scaffolds reinforced with baghdadite-magnetite nanoparticles using a 3D printer and freeze-drying technique, J. Mater. Res. Technol. 14 (2021) 3070–3079.
[27] X. Dong, A. Heidari, A. Mansouri, W.S. Hao, M. Dehghani, S. Saber-Samandari, D. Toghraie, A. Khandan, Investigation of the mechanical properties of a bony scaffold for comminuted distal radial fractures: addition of akermanite nanoparticles and using a freeze-drying technique, J. Mech. Behav. Biomed. Mater. 121 (2021) 104643.
[28] Z. Abbas, M. Dapporto, A. Tampieri, S. Sprio, Toughening of bioceramic composites for bone regeneration, J. Compos. Sci. 5 (2021) 259.
[29] H. Inam, S. Sprio, M. Tavoni, Z. Abbas, F. Pupilli, A. Tampieri, Magnetic hydroxyapatite nanoparticles in regenerative medicine and nanomedicine, Int. J. Mol. Sci. 25 (2024) 2809.
[30] Z. Abbas, M. Dapporto, A. Piancastelli, D. Gardini, A. Tampieri, S. Sprio, Rheological behavior of ion-doped hydroxyapatite slurries, J. Compos. Sci. 9 (2025) 181.
[31] A. Zimina, F. Senatov, R. Choudhary, E. Kolesnikov, N. Anisimova, M. Kiselevskiy, P. Orlova, N. Strukova, M. Generalova, V. Manskikh, Biocompatibility and physico-chemical properties of highly porous PLA/HA scaffolds for bone reconstruction, Polymers 12 (2020) 2938.
[32] W. Wang, B. Zhang, L. Zhao, M. Li, Y. Han, L. Wang, Z. Zhang, J. Li, C. Zhou, L. Liu, Fabrication and properties of PLA/nano-HA composite scaffolds with balanced mechanical properties and biological functions for bone tissue engineering application, Nanotechnol. Rev. 10 (2021) 1359–1373.
[33] P. Feng, J. Jia, M. Liu, S. Peng, Z. Zhao, C. Shuai, Degradation mechanisms and acceleration strategies of poly (lactic acid) scaffold for bone regeneration, Mater. Des. 210 (2021) 110066.
[34] W. Wang, B. Zhang, M. Li, J. Li, C. Zhang, Y. Han, L. Wang, K. Wang, C. Zhou, L. Liu, 3D printing of PLA/n-HA composite scaffolds with customized mechanical properties and biological functions for bone tissue engineering, Compos. B Eng. 224 (2021) 109192.
[35] B. Zhang, L. Wang, P. Song, X. Pei, H. Sun, L. Wu, C. Zhou, K. Wang, Y. Fan, X. Zhang, 3D printed bone tissue regenerative PLA/HA scaffolds with comprehensive performance optimizations, Mater. Des. 201 (2021) 109490.
[36] S. Hassanajili, A. Karami-Pour, A. Oryan, T. Talaei-Khozani, Preparation and characterization of PLA/PCL/HA composite scaffolds using indirect 3D printing for bone tissue engineering, Mater. Sci. Eng.: C 104 (2019) 109960.
[37] Plasma biotal, https://www.plasma-biotal.com/captal-r-hydroxylapatite/, (Accessed January 2025).
[38] M. Mohammadi, B. Coppola, L. Montanaro, P. Palmero, Digital light processing of high-strength hydroxyapatite ceramics: role of particle size and printing parameters on microstructural defects and mechanical properties, J. Eur. Ceram. Soc. 43 (2023) 2761–2772, https://doi.org/10.1016/j.jeurceramsoc.2022.11.047.
[39] Uniformatio3D, https://uniformation3d.com/products/uniformation-pla-plant-based-resin-x15-transparent, (Accessed January 2025).
[40] ISO 604:2002 Plastics — Determination of compressive properties, https://www.iso.org/standard/31261.html, (Accessed January 2025).
[41] https://admateceurope.com/admaflex130, (Accessed January 2025).
[42] A.B. Saed, A.H. Behravesh, S. Hasannia, S.A.A. Ardebili, B. Akhoundi, M. Pourghayoumi, Functionalized poly L-lactic acid synthesis and optimization of process parameters for 3D printing of porous scaffolds via digital light processing (DLP) method, J. Manuf. Process. 56 (2020) 550–561.
[43] N. Baumann, K.M. Diaz, K. Simmons-Potter, B.G. Potter Jr, J. Bucay, Particle loading as a design parameter for composite radiation shielding, Nucl. Eng. Technol. 54 (2022) 3855–3863.
[44] D. Wu, A. Spanou, A. Diez-Escudero, C. Persson, 3D-printed PLA/HA composite structures as synthetic trabecular bone: a feasibility study using fused deposition modeling, J. Mech. Behav. Biomed. Mater. 103 (2020) 103608.
[45] N. Thadavirul, P. Pavasant, P. Supaphol, Fabrication and evaluation of polycaprolactone–poly (hydroxybutyrate) or poly (3-hydroxybutyrate-co-3-hydroxyvalerate) dual-leached porous scaffolds for bone tissue engineering applications, Macromol. Mater. Eng. 302 (2017) 1600289.
[46] C. Hinczewski, S. Corbel, T. Chartier, Ceramic suspensions suitable for stereolithography, J. Eur. Ceram. Soc. 18 (1998) 583–590.
[47] A.M.M. Amin, D.H.A. Besisa, A.A.M. El-Amir, Z.I. Zaki, Y.M.Z. Ahmed, Role of heat treatment of hydroxyapatite powder prior to suspension preparation on the suspension flow behavior, Open Ceram. 9 (2022) 100239.
[48] A.V.M. Esteves, M.I. Martins, P. Soares, M.A. Rodrigues, M.A. Lopes, J.D. Santos, Additive manufacturing of ceramic alumina/calcium phosphate structures by DLP 3D printing, Mater. Chem. Phys. 276 (2022) 125417.
[49] J.O. Akindoyo, M.D.H. Beg, S. Ghazali, H.P. Heim, M. Feldmann, Impact modified PLA-hydroxyapatite composites – thermo-mechanical properties, Compos. Part A Appl. Sci. Manuf. 107 (2018) 326–333, https://doi.org/10.1016/j.compositesa.2018.01.017.
[50] A.A. Sheader, P.D. Nellist, Use of partial scattering EDX cross-sections to quantify light elements in the STEM, Microsc. Microanal. 28 (2022) 2448–2450, https://doi.org/10.1017/S1431927622009382.
[51] H.K. Yerli, K. Cava, M. Aslan, Characterisation of 3D printed hydroxyapitate powder (HAp) filled polylactic acid (PLA) composites, Int. J. 3D Print. Technol. Digit. Ind. 6 (2022) 540–547.
[52] J.O. Akindoyo, M.D.H. Beg, S. Ghazali, H.P. Heim, M. Feldmann, Effects of surface modification on dispersion, mechanical, thermal and dynamic mechanical properties of injection molded PLA-hydroxyapatite composites, Compos. Part A Appl. Sci. Manuf. 103 (2017) 96–105, https://doi.org/10.1016/j.compositesa.2017.09.013.
[53] R. Zhang, H. Hu, Y. Liu, J. Tan, W. Chen, C. Ying, Q. Liu, X. Fu, S. Hu, C.P. Wong, Homogeneously dispersed composites of hydroxyapatite nanorods and poly(lactic acid) and their mechanical properties and crystallization behavior, Compos. Part A Appl. Sci. Manuf. 132 (2020) 105841, https://doi.org/10.1016/j.compositesa.2020.105841.
[54] B.M. Kennedy, E. De Barra, S. Hampshire, M.C. Kelleher, Investigation of oleic acid as a dispersant for hydroxyapatite powders for use in ceramic filled photo-curable resins for stereolithography, J. Eur. Ceram. Soc. 43 (2023) 7146–7166, https://doi.org/10.1016/j.jeurceramsoc.2023.07.028.
[55] A.B. Saed, A.H. Behravesh, S. Hasannia, B. Akhoundi, S.K. Hedayati, F. Gashtasbi, An in vitro study on the key features of Poly L-lactic acid/biphasic calcium phosphate scaffolds fabricated via DLP 3D printing for bone grafting, Eur. Polym. J. 141 (2020) 110057, https://doi.org/10.1016/j.eurpolymj.2020.110057.
[56] G. Dal Poggetto, U. D'Amora, A. Ronca, M.G. Raucci, A. Soriente, G. Gomez d'Ayala, P. Laurienzo, Chemical modification of PLA for the design of 3D printed nanocomposite scaffolds with enhanced degradability for bone tissue engineering, Polym. Compos. (2025).
[57] J.C. de Andrade, F. Cabral, F.J. Clemens, J.L. Vieira, M.B.P. Soares, D. Hotza, M. C. Fredel, Effect of stearic acid on the mechanical and rheological properties of PLA/HA biocomposites, Mater. Today Commun. 35 (2023) 106357.
[58] B.S. Heidari, E.M. Lopez, P. Chen, R. Ruan, E. Vahabli, S.M. Davachi, F. Granero-Moltó, E.M. De-Juan-Pardo, M. Zheng, B. Doyle, Silane-modified hydroxyapatite nanoparticles incorporated into polydioxanone/poly(lactide-co-caprolactone) creates a novel toughened nanocomposite with improved material properties and in vivo inflammatory responses, Mater. Today Bio 22 (2023) 100778, https://doi.org/10.1016/j.mtbio.2023.100778.
[59] J. Li, X.L. Lu, Y.F. Zheng, Effect of surface modified hydroxyapatite on the tensile property improvement of HA/PLA composite, Appl. Surf. Sci. 255 (2008) 494–497.
[60] C.R. Rocha, D. Chávez-Flores, N. Zuverza-Mena, A. Duarte, B.A. Rocha-Gutiérrez, E.A. Zaragoza-Contreras, S. Flores-Gallardo, Surface organo-modification of hydroxyapatites to improve PLA/HA compatibility, J. Appl. Polym. Sci. 137 (2020) 49293.
[61] M. Khamvongsa, K. Milton, T.R. Faisal, Mechanical characterization of low-cost 3D FDM printed scaffolds fabricated with synthesized PLA/HA bio-composite filament, Ann. 3D Printed Med. (2025) 100194.
[62] H. Wang, J. Zhang, H. Bai, C. Wang, Z. Li, Z. Wang, Q. Liu, Z. Wang, X. Wang, X. Zhu, 3D printed cell-free bilayer porous scaffold based on alginate with biomimetic microenvironment for osteochondral defect repair, Biomater. Adv. 167 (2025) 214092.
[63] S. Álvarez-Olcina, M. López-Álvarez, J. Serra, P. González, Iron-oxide nanoparticles embedded in 3D-printed PLA/HA scaffolds for magnetic hyperthermia therapy: an experimental–numerical analysis of thermal behavior, Materials 17 (2024) 5836.
[64] A.J.R.L. Rodovalho, W.T. Barbosa, J.L. Vieira, C.A. de Oliva, A.P.B. Gonçalves, P.d. S.M. Cardoso, H.B. Modolon, O.R.K. Montedo, S. Arcaro, K.V.S. Hodel, Influence of size and crystallinity of nanohydroxyapatite (nHA) particles on the properties of Polylactic Acid/nHA nanocomposite scaffolds produced by 3D printing, J. Mater. Res. Technol. 30 (2024) 3101–3111.
[65] S. Pérez-Davila, N. Garrido-Gulías, L. González-Rodríguez, M. López-Álvarez, J. Serra, J.E. López-Periago, P. González, Physicochemical properties of 3D-printed polylactic acid/hydroxyapatite scaffolds, Polymers 15 (2023) 2849.
[66] M. He, F. Zhang, C. Li, Y. Su, Z. Qin, Y. Niu, W. Shang, B. Liu, Mechanical properties and oral restoration applications of 3D printed aliphatic polyester-calcium composite materials, Alexand. Eng. J. 88 (2024) 245–252.
[67] M. Bayart, M. Dubus, S. Charlon, H. Kerdjoudj, N. Baleine, S. Benali, J.-M. Raquez, J. Soulestin, Pellet-Based fused filament fabrication (FFF)-derived process for the development of polylactic acid/hydroxyapatite scaffolds dedicated to bone regeneration, Materials 15 (2022) 5615.
[68] S. Sahmani, A. Khandan, S. Saber-Samandari, S. Esmaeili, M.M. Aghdam, Fabrication and resonance simulation of 3D-printed biocomposite mesoporous implants with different periodic cellular topologies, Bioprinting 22 (2021) e00138.
[69] C. Prakash, G. Singh, S. Singh, W.L. Linda, H.Y. Zheng, S. Ramakrishna, R. Narayan, Mechanical reliability and in vitro bioactivity of 3D-printed porous polylactic acid-hydroxyapatite scaffold, J. Mater. Eng. Perform. 30 (2021) 4946–4956.
[70] K. Thunsiri, S. Pitjamit, P. Pothacharoen, D. Pruksakorn, W. Nakkiew, W. Wattanutchariya, The 3D-printed bilayer's bioactive-biomaterials scaffold for full-thickness articular cartilage defects treatment, Materials 13 (2020) 3417.
[71] F. Liu, Y. Wang, J. Cao, J. Chen, T. Luo, C. Zhou, Y. Tang, H. Xie, A simple method for fabricating polymer/ceramic functionally graded material scaffold, Ceram. Int. 50 (2024) 14497–14512.
[72] E. Mancini, M. Utzeri, E. Farotti, A. Lattanzi, M. Sasso, DLP printed 3D gyroid structure: mechanical response at meso and macro scale, Mech. Mater. 192 (2024) 104970.
[73] L.J. Gibson, M.F. Ashby, Cellular Solids: Structure and Properties, 2nd ed., Cambridge University Press, Cambridge, 1997 https://doi.org/10.1017/CBO9781139878326.
[74] T. Maconachie, R. Tino, B. Lozanovski, M. Watson, A. Jones, C. Pandelidi, A. Alghamdi, A. Almalki, D. Downing, M. Brandt, The compressive behaviour of

ABS gyroid lattice structures manufactured by fused deposition modelling, Int. J. Adv. Manufac. Technol. 107 (2020) 4449–4467.
[75] D.W. Abueidda, M. Elhebeary, C.-S.A. Shiang, S. Pang, R.K.A. Al-Rub, I.M. Jasiuk, Mechanical properties of 3D printed polymeric gyroid cellular structures: experimental and finite element study, Mater. Des. 165 (2019) 107597.
[76] V. Trakoolwannachai, P. Kheolamai, S. Ummartyotin, Characterization of hydroxyapatite from eggshell waste and polycaprolactone (PCL) composite for scaffold material, Compos. B Eng. 173 (2019) 106974, https://doi.org/10.1016/j.compositesb.2019.106974.
[77] M.P. Bernardo, B.C.R. da Silva, A.E.I. Hamouda, M.A.S. de Toledo, C. Schalla, S. Rütten, R. Goetzke, L.H.C. Mattoso, M. Zenke, A. Sechi, PLA/Hydroxyapatite scaffolds exhibit in vitro immunological inertness and promote robust osteogenic differentiation of human mesenchymal stem cells without osteogenic stimuli, Sci. Rep. 12 (2022) 2333.
[78] P. Wiecinska, M. Bachonko, Processing of porous ceramics from highly concentrated suspensions by foaming, in situ polymerization and burn-out of polylactide fibers, Ceram. Int. 42 (2016) 15057–15064, https://doi.org/10.1016/j.ceramint.2016.06.162.
[79] N. Uysal, G. Acik, M.A. Tasdelen, Soybean oil based thermoset networks via photoinduced CuAAC click chemistry, Polym. Int. 66 (2017) 999–1004.
[80] X. Niu, N. Li, Z. Du, X. Li, Integrated gradient tissue-engineered osteochondral scaffolds: challenges, current efforts and future perspectives, Bioact. Mater. 20 (2023) 574–597, https://doi.org/10.1016/j.bioactmat.2022.06.011.
[81] W. Guo, Z. Jiang, H. Zhong, G. Chen, X. li, H. Yan, C. Zhang, L. Zhao, 3D printing of multifunctional gradient bone scaffolds with programmable component distribution and hierarchical pore structure, Compos. Part A Appl. Sci. Manuf. 166 (2023) 107361, https://doi.org/10.1016/j.compositesa.2022.107361.
[82] R. Chen, J.S. Pye, J. Li, C.B. Little, J.J. Li, Multiphasic scaffolds for the repair of osteochondral defects: outcomes of preclinical studies, Bioact. Mater. 27 (2023) 505–545, https://doi.org/10.1016/j.bioactmat.2023.04.016.
[83] S.W. Chan, N. Jusoh, A.A. Samad, Effect of fluid properties on bone scaffold permeability, in: International Conference for Innovation in Biomedical Engineering and Life Sciences, Springer, 2022, pp. 21–29.